

Excess TGF- β mediates muscle weakness associated with bone metastases in mice

David L Waning^{1,9}, Khalid S Mohammad^{1,9}, Steven Reiken², Wenjun Xie², Daniel C Andersson^{2,8}, Sutha John¹, Antonella Chiechi¹, Laura E Wright¹, Alisa Umanskaya², Maria Niewolna¹, Trupti Trivedi¹, Sahba Charkhzarrin¹, Pooja Khatiwada¹, Anetta Wronska², Ashley Haynes², Maria Serena Benassi³, Frank A Witzmann⁴, Gehua Zhen⁵, Xiao Wang⁵, Xu Cao⁵, G David Roodman^{6,7}, Andrew R Marks² & Theresa A Guise¹

Cancer-associated muscle weakness is a poorly understood phenomenon, and there is no effective treatment. Here we find that seven different mouse models of human osteolytic bone metastases—representing breast, lung and prostate cancers, as well as multiple myeloma—exhibited impaired muscle function, implicating a role for the tumor-bone microenvironment in cancer-associated muscle weakness. We found that transforming growth factor (TGF)- β , released from the bone surface as a result of metastasis-induced bone destruction, upregulated NADPH oxidase 4 (Nox4), resulting in elevated oxidation of skeletal muscle proteins, including the ryanodine receptor and calcium (Ca²⁺) release channel (RyR1). The oxidized RyR1 channels leaked Ca²⁺, resulting in lower intracellular signaling, which is required for proper muscle contraction. We found that inhibiting RyR1 leakage, TGF- β signaling, TGF- β release from bone or Nox4 activity improved muscle function in mice with MDA-MB-231 bone metastases. Humans with breast- or lung cancer-associated bone metastases also had oxidized skeletal muscle RyR1 that is not seen in normal muscle. Similarly, skeletal muscle weakness, increased Nox4 binding to RyR1 and oxidation of RyR1 were present in a mouse model of Camurati-Engelmann disease, a nonmalignant metabolic bone disorder associated with increased TGF- β activity. Thus, pathological TGF- β release from bone contributes to muscle weakness by decreasing Ca²⁺-induced muscle force production.

Skeletal muscle weakness is a debilitating consequence of advanced malignancies, which are often associated with bone metastases. Research and therapy have focused on increasing muscle mass in humans with cancer-associated skeletal muscle weakness¹, but it is unclear whether a gain of mass alone will improve muscle function^{2,3}. Moreover, little is known about whether tumors and their associated metastases cause muscle dysfunction resulting in weakness, or whether cancer-associated weakness is due solely to loss of muscle mass. Therefore, using mouse models of human cancers with bone metastases, we investigated whether there is a cause of muscle weakness that is independent of muscle mass loss.

Individuals with advanced cancer (including those of the breast, prostate and lung), often have bone metastases and muscle weakness. In the tumor-bone microenvironment, cancer cells (including those in individuals with multiple myeloma) secrete factors that stimulate osteoclastic bone resorption, resulting in skeletal complications of bone pain, fractures, hypercalcemia, nerve compression syndromes and muscle weakness⁴. Osteoclastic bone resorption releases growth factors stored in the bone matrix, principally TGF- β , that further promote cancer cell invasion, growth

and osteolytic factor production to fuel a feed-forward cycle that induces more bone destruction and tumor growth^{4–7}. Bone resorption and formation is dynamically coupled by TGF- β (ref. 8), and pathologically increased TGF- β release from bone, due to tumor-induced osteolysis, could be contributing to muscle weakness. Here we found that mouse models of human breast, lung and prostate cancers, as well as a mouse model of multiple myeloma, in which all mice develop osteolytic bone metastases and exhibit profound skeletal muscle weakness. We report that pathologically increased TGF- β release from bone causes muscle weakness by inducing intracellular Ca²⁺ leakage via Nox4-mediated oxidation of RyR1 on the sarcoplasmic reticulum (SR).

In normal muscle, activation of RyR1 results in the release of SR Ca²⁺ that is the required signal to trigger skeletal muscle contraction⁹. Pathological oxidation of RyR1 results in leaky channels that contribute to muscle weakness¹⁰. Here we show that targeting intracellular Ca²⁺ leakage, bone resorption, TGF- β activity and Nox4 activity can all prevent muscle weakness in mice with breast cancer-derived bone metastases. Furthermore, increased Nox4 binding to RyR1, oxidation of RyR1 and muscle weakness were observed in a mouse model of

¹Department of Medicine, Indiana University School of Medicine, Indianapolis, Indiana, USA. ²Department of Physiology and Cellular Biophysics, Helen and Clyde Wu Center for Molecular Cardiology, College of Physicians and Surgeons, Columbia University, New York, New York, USA. ³Laboratory of Experimental Oncology, Istituto Ortopedico Rizzoli, Bologna, Italy. ⁴Department of Cellular and Integrative Physiology, Indiana University School of Medicine, Indianapolis, Indiana, USA. ⁵Department of Orthopedic Surgery, Johns Hopkins University School of Medicine, Baltimore, Maryland, USA. ⁶Department of Medicine, Division of Hematology and Oncology, Indiana University School of Medicine, Indianapolis, Indiana, USA. ⁷Richard L. Roudebush Virginia Medical Center, Indianapolis, Indiana, USA. ⁸Present addresses: Department of Medicine, Cardiology Unit, Karolinska Institute, Stockholm, Sweden, and Department of Physiology and Pharmacology, Karolinska Institute, Stockholm, Sweden (D.C.A.). ⁹These authors contributed equally to this work. Correspondence should be addressed to T.A.G. (tguise@iu.edu).

Received 3 April; accepted 2 September; published online 12 October 2015; doi:10.1038/nm.3961

Camurati-Engelmann disease (CED), a nonmalignant metabolic bone disorder associated with increased TGF- β activity and bone destruction.

These findings raise the possibility that increased bone destruction and associated elevations in TGF- β activity can induce skeletal muscle weakness by the oxidation of RyR1 and the resultant Ca²⁺ leakage. Thus, targeting any portion of this pathway might help to ameliorate muscle weakness in cancer patients with bone metastases.

RESULTS

Weakness and RyR1 oxidation in mice with bone metastases

To explore the basis for cancer-associated muscle weakness, we used a mouse model of human breast cancer (MDA-MB-231) that causes osteolytic bone metastases and muscle weakness (**Supplementary Fig. 1a**)¹¹. We inoculated 5-week-old female nude mice with 100,000 MDA-MB-231 human breast cancer cells via the left cardiac ventricle and found that these mice had bone metastases, lower skeletal muscle mass and reduced body weight, fat and lean content (**Supplementary Fig. 1b**) 4 weeks post-tumor inoculation as compared to tumor-free (non-tumor) control mice (**Supplementary Fig. 1c,d**). As compared to the non-tumor control mice, the tumor-bearing mice developed muscle weakness (reduction in forelimb grip strength) (**Fig. 1a**), and the extensor digitorum longus (EDL) muscle showed lower *ex vivo* muscle-specific force (which represents the muscle force corrected for changes in muscle size) (**Fig. 1b**). Peak tetanic Ca²⁺ determines muscle force, and we found that this was also lower in the MDA-MB-231-inoculated mice than in the non-tumor-bearing control mice (**Fig. 1c**). Thus, in addition to loss of muscle mass, mice with breast cancer bone metastases had loss of muscle function.

Advanced breast cancer is characterized by increased oxidative stress¹². We used an unbiased mass spectrometry-based screen to assess post-translational modifications of proteins in whole skeletal muscle lysates from mice with bone metastases as compared to those from non-tumor-bearing controls (**Supplementary Tables 1 and 2**). Measurement of the total carbonyl concentration in skeletal muscle lysates also showed that skeletal muscle from mice and humans with tumors metastatic to bone exhibited higher skeletal muscle protein oxidation as compared to muscle from mice and humans without bone metastases (**Supplementary Table 3**). We found that proteins involved in muscle contraction were among the skeletal muscle proteins that were nitrosylated or oxidized in mice with bone metastases (**Supplementary Tables 1 and 2**). These included sarcomeric proteins (such as tropomyosin and myosin) and the RyR1 Ca²⁺ release channel, which was identified as being both nitrosylated and oxidized (**Supplementary Tables 1 and 2**). Because tetanic Ca²⁺ was lower in mice with MDA-MB-231 bone metastases than in non-tumor control mice, we focused on RyR1, as this channel is the source of Ca²⁺ release from the SR in skeletal muscle. Oxidation of RyR1 channels in skeletal muscle results in a pathological SR Ca²⁺ leak that is associated with muscle weakness^{10,13}. Indeed, skeletal muscle RyR1 channels from mice with bone metastases were oxidized, nitrosylated and depleted of the stabilizing subunit calstabin1 (also known as FKBP12) as compared to that from non-tumor control mice (the biochemical signature of leaky channels) (**Fig. 1d**). These oxidation-induced changes in RyR1 were progressive over 4 weeks after tumor inoculation during the development of bone metastases (**Supplementary Fig. 1e**) and were associated with lower muscle-specific force in mice with breast cancer bone metastases than in non-tumor control mice (**Supplementary Fig. 1f**). Mice with MDA-MB-231 breast cancer bone metastases had large osteolytic lesions, as determined by analysis of X-ray images, and the degree of muscle weakness

correlated with the amount of bone destruction 4 weeks after tumor inoculation (**Supplementary Fig. 1g,h**). To determine whether the RyR1 modifications observed in the mouse models were relevant to human cancer, we examined skeletal muscle RyR1 from humans with breast cancer-associated bone metastases or lung cancer-associated bone metastases and compared them to those from humans who did not have cancer and found the same post-translational modifications (oxidation and nitrosylation of RyR1 and lower calstabin1 binding) as we observed in the mouse models, which we hereafter refer to as the biochemical signature of leaky RyR1 channels (**Fig. 1e,f**).

Muscle weakness associated with bone metastases

Because muscle weakness strongly correlated with bone destruction (**Supplementary Fig. 1h**), we investigated whether the tumor-bone microenvironment plays a role in cancer-associated muscle weakness. We inoculated 1×10^6 MDA-MB-231 cells (tenfold more cells than were used in the bone metastasis model) into the mammary fat pad (inoculation into which causes primary breast cancer only¹⁴ and no bone metastases) and found that, in contrast to mice with bone metastases, mice with primary MDA-MB-231 mammary tumors (mean tumor mass 400 ± 91 mg) had normal muscle function (**Fig. 1g**), muscle mass, body weight and body composition (**Supplementary Fig. 1i,j**). Notably, these mice did not exhibit the biochemical signature of leaky RyR1 channels, in contrast to mice with bone metastases (**Fig. 1h**). These data suggest that the tumor-bone microenvironment has a critical role in the development of cancer-associated muscle weakness.

Here we examined mice with bone metastases resulting from seven different forms of human cancers, including MDA-MB-231 breast cancer, MCF-7 breast cancer, ZR75-1 breast cancer, A549 lung cancer, RWGT2 lung cancer¹⁵, PC-3 prostate cancer and JJN-3 multiple myeloma, and we compared the results obtained from each group of mice with those from non-tumor control mice. We sought to determine whether muscle weakness and oxidative modifications of RyR1 are common features of diverse malignancies that are associated with bone destruction (osteolysis). These cancer models have bone metastases that are associated with components of osteolysis (except for ZR75-1, which is osteoblastic). Similarly to mice with MDA-MB-231 breast cancer bone metastases, mice with osteolytic or mixed osteolytic and osteoblastic bone metastases (i.e., with components of both bone destruction and bone formation) also had lower EDL *ex vivo* muscle-specific force than did non-tumor control mice.

Mice with A549 human lung cancer bone metastases had osteolytic bone destruction, reduced forelimb grip strength and lower *ex vivo* muscle-specific force generation of the EDL than in non-tumor control mice (**Supplementary Fig. 2a**). Similarly to mice with MDA-MB-231 breast cancer bone metastases, we observed that A549 inoculation resulted in mice with lower muscle weights (EDL, tibialis anterior, soleus and gastrocnemius) and reduced body weight owing to loss of both lean and fat mass as compared to non-tumor control mice (**Supplementary Fig. 2b**). Skeletal muscle RyR1 channels from mice with A549 lung cancer bone metastases also exhibited the biochemical signature of leaky channels^{10,13}, as observed with skeletal muscle RyR1 from MDA-MB-231 mice (**Supplementary Fig. 2c**). RWGT2 human lung cancer bone metastases¹⁵ caused mixed osteolytic and osteoblastic lesions in bone, and these mice had lower EDL *ex vivo* muscle-specific force but without reduced forelimb grip strength as compared to non-tumor control mice (**Supplementary Fig. 2d**). RWGT2 did not lower skeletal muscle weight (with the exception of the soleus), reduce whole body weight, alter body composition or lower

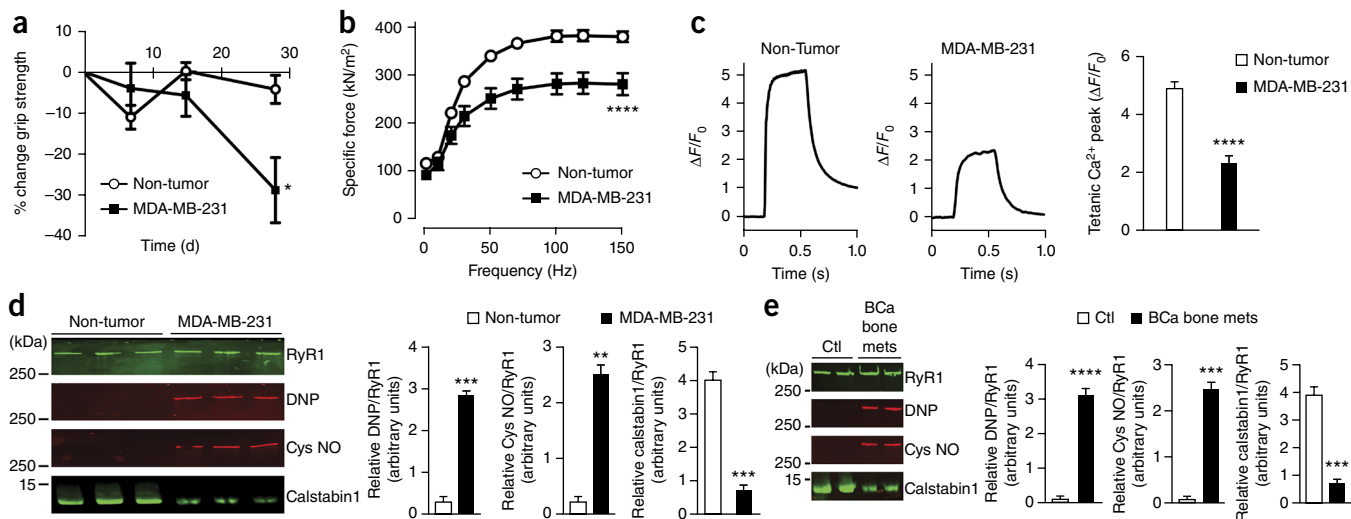


Figure 1 Skeletal muscle weakness is due to breast cancer bone metastases. (a,b) *In vivo* forelimb grip strength ($n = 10$) (a) and *ex vivo* specific force of the extensor digitorum longus (EDL) muscle ($n = 10$) (b) in mice with MDA-MB-231 breast cancer bone metastases. (c) Tetanic Ca^{2+} peak (measured by using the Ca^{2+} -sensitive fluorescent dye Fluo-4 (ΔF , change in fluorescence; $\Delta F/F_0$, resting signal)) in isolated flexor digitorum brevis (FDB) muscle fibers. Representative single traces (left) and quantification from $n = 25$ fibers (right). (d) Immunoblot (left) and quantification (right) of RyR1 oxidation (DNP) and nitrosylation (Cys NO) and of RyR1-calstabin1 binding, as measured by coimmunoprecipitation, from EDL muscle ($n = 3$). (e,f) Immunoblot (left) and quantification (right) of RyR1 oxidation and nitrosylation and of RyR1-calstabin1 binding in muscle samples from humans with breast cancer bone metastases (BCa bone mets) (e) or lung cancer bone metastases (LCa bone mets) (f) and their respective controls (Ctl); $n = 4$ per group. (g) *Ex vivo* EDL specific force in mice with primary MDA-MB-231 breast cancer as compared to that in non-tumor control mice ($n = 9$). (h) Immunoblot (left) and quantification (right) of RyR1 oxidation and nitrosylation and of RyR1-calstabin1 binding in mice with primary breast cancer ($n = 4$ per group). SR + H_2O_2 , sarcoplasmic reticulum preparations treated with hydrogen peroxide. Data are mean \pm s.e.m. Statistical analysis in a,b,g was by two-way analysis of variance (ANOVA) and in c–f was by Student's *t*-test. * $P < 0.05$, ** $P < 0.01$, *** $P < 0.001$, **** $P < 0.0001$.

mid-calf cross-sectional area as compared to that observed in non-tumor control mice (Supplementary Fig. 2e); however, these mice did exhibit RyR1 modifications similarly to those seen in mice with MDA-MB-231 breast cancer bone metastases (Supplementary Fig. 2f).

Mice with MCF-7 breast cancer-associated bone metastases, which have osteolytic and osteoblastic (mixed) components, also had lower EDL *ex vivo* muscle-specific force than non-tumor control mice (Supplementary Fig. 2g). As compared to non-tumor control animals, mice with MCF-7-associated bone metastases did not have lower muscle weight but did lose total body weight (Supplementary Fig. 2h). Skeletal muscle RyR1 channels from mice with MCF-7 breast cancer and bone metastases also exhibited the same biochemical signature of leaky channels as that observed in MDA-MB-231 tumor-bearing mice with bone metastases (Supplementary Fig. 2i).

PC-3 human prostate cancer tumor-bearing mice showed osteolytic metastases, reduction in forelimb grip strength and lower EDL *ex vivo* muscle-specific force in comparison with non-tumor control mice (Supplementary Fig. 3a). As compared to the control mice, these mice also had lower muscle weight, reduced

body weight and lower fat and lean mass (Supplementary Fig. 3b), and they showed the biochemical signature of leaky RyR1 channels (Supplementary Fig. 3c).

Direct inoculation of human JJN-3 multiple myeloma cells into the tibias of mice caused bone destruction as previously described¹⁶ but no loss of body weight. Mice with JJN-3 multiple myeloma, as compared to non-tumor control mice, had lower *ex vivo* muscle-specific force of the EDL (measured in the contralateral limb), and their RyR1 channels exhibited the biochemical signature of leaky channels (Supplementary Fig. 3d). JJN-3 multiple myeloma-induced bone destruction (osteolytic lesion area) correlated with decreased specific force of the EDL in the contralateral limb (without decreased muscle mass or body weight) compared to non-tumor control mice, indicating once again that local bone destruction in the tumor-bone microenvironment can cause systemic muscle weakness (Supplementary Fig. 3e).

In contrast to non-tumor control animals, mice injected with ZR75-1 human breast cancer cells had bone metastases with abnormal new bone formation but without bone destruction (osteoblastic), as well as lower EDL *ex vivo* muscle-specific force but not reduced forelimb

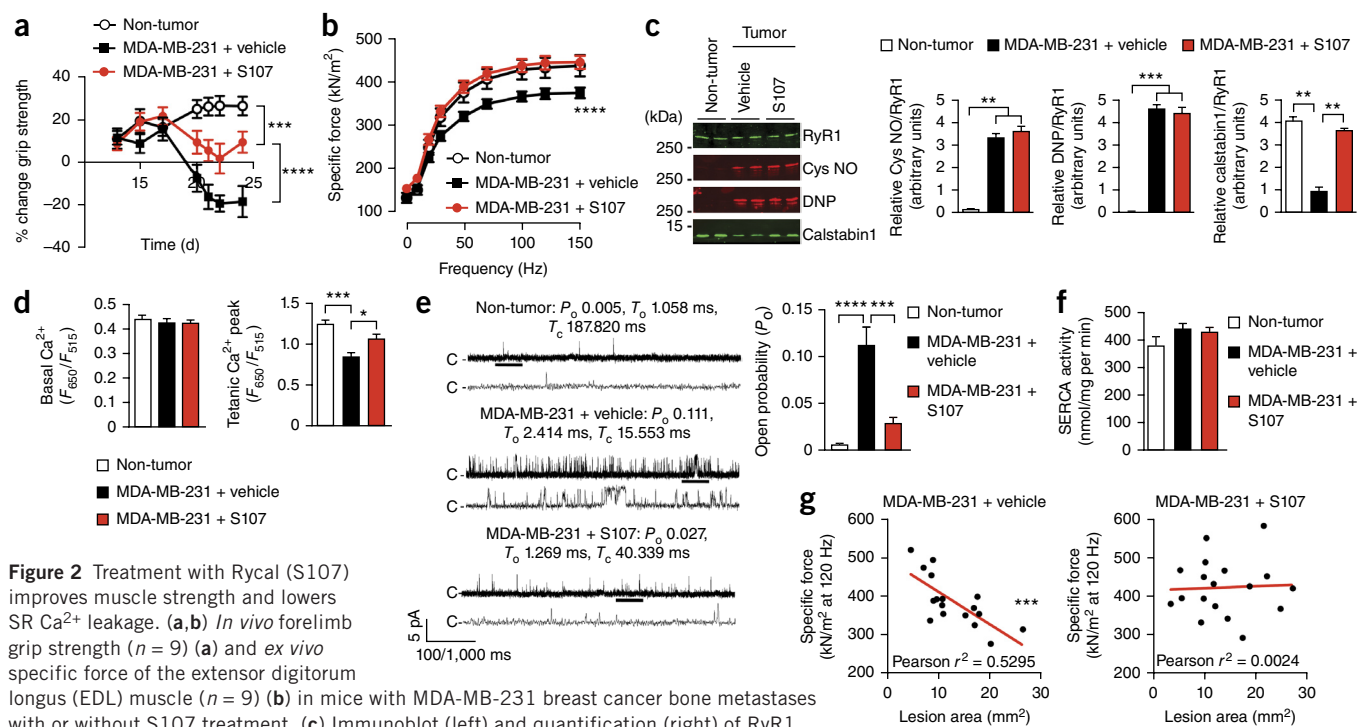


Figure 2 Treatment with Rycal (S107) improves muscle strength and lowers SR Ca^{2+} leakage. **(a,b)** *In vivo* forelimb grip strength ($n = 9$) **(a)** and *ex vivo* specific force of the extensor digitorum longus (EDL) muscle ($n = 9$) **(b)** in mice with MDA-MB-231 breast cancer bone metastases with or without S107 treatment. **(c)** Immunoblot (left) and quantification (right) of RyR1 oxidation (DNP) and nitrosylation (Cys NO) and of RyR1-calstabin1 binding, as measured by coimmunoprecipitation, from EDL muscle ($n = 4$). **(d)** Peak tetanic Ca^{2+} amplitude in mice with MDA-MB-231 bone metastases receiving S107 treatment (ratiometric imaging using the Ca^{2+} fluorescent dyes Fluo-4 and Fura-red to obtain an $F_{650\text{ nm}}/F_{515\text{ nm}}$ ratio, reflecting the absolute Ca^{2+} level) in flexor digitorum brevis (FDB) muscle fibers ($n = 36$ fibers). **(e)** RyR1 channel open probability in muscle from mice with MDA-MB-231 bone metastases receiving S107 treatment. Left, representative single-channel current traces of skeletal RyR1 channels ($n = 4$). Channel openings are shown as upward deflections. P_o , open probability; T_o , average open time; T_c , average closed time. The activity of the channel, as indicated by the thick black bar, is shown below on the expanded time scale. Right, quantification of traces from $n = 4$ channel recordings. **(f)** SERCA activity from muscle of mice with bone metastases and treated with S107 ($n = 4$). **(g)** Correlation between maximum specific force (120 Hz) and osteolytic lesion area (as measured in all limbs by X-ray imaging) in muscle from mice with MDA-MB-231 bone metastases that were treated with vehicle or S107. Data are mean \pm s.e.m. Statistical analysis in **a,b** was by two-way ANOVA, in **c-f** was by one-way ANOVA with multiple comparisons and in **g** by Pearson's correlation. * $P < 0.05$, ** $P < 0.01$, *** $P < 0.001$, **** $P < 0.0001$.

grip strength (**Supplementary Fig. 3f**). There was no loss of muscle weight or whole body weight, nor did the mice have changes in body composition, although mid-calf cross-sectional area was higher than in non-tumor control mice (**Supplementary Fig. 3g**), and we did not observe RyR1 modifications (**Supplementary Fig. 3h**).

Taken together, these data show that, as compared to non-tumor control animals, mice with predominantly osteolytic (MDA-MB-231 breast cancer, A549 lung cancer, PC3 prostate cancer and JJN3 multiple myeloma) and mixed osteolytic and osteoblastic bone metastases (RWGT2 lung cancer and MCF-7 breast cancer) showed lower muscle-specific force production, lower muscle strength and RyR1 modifications that are consistent with leaky channels, regardless of whether there was weight loss or reduced muscle mass as compared to that in non-tumor control mice. In contrast, mice with ZR75-1 breast cancer cells showed induction of osteoblastic bone metastases and lower muscle function but no modification of RyR1 as compared to non-tumor control mice. Of note, it takes 7 months for the ZR75-1 mice to develop bone metastases and muscle weakness, as opposed to 4–12 weeks for the same development in all of the other models we examined. The lower muscle force production in the ZR75-1 mice occurs in the absence of bone destruction and without RyR1 modifications, suggesting a mechanism distinct from the other forms of cancer in bone.

Inhibiting RyR1 Ca^{2+} leak improves muscle strength

The clinical relevance of the leaky RyR1 modifications in skeletal muscle from mice with osteolytic bone metastases is reinforced because we

found the same biochemical signature of leaky RyR1 channels in skeletal muscle from humans with osteolytic breast or lung cancer that was metastatic to bone (**Fig. 1e,f**). The RyR1 Ca^{2+} release channel stabilizer Rycal (S107) is a small molecule in the 1,4-benzothiazepine family whose structure and properties have been previously published¹⁷. S107 fixes leaky RyR1 channels by inhibiting oxidation-induced depletion of the channel-stabilizing subunit calstabin1 from the RyR1 complex, which stabilizes the closed state of the channel and prevents aberrant intracellular Ca^{2+} leak, thereby improving the Ca^{2+} signal for muscle force production and enhancing muscle strength and exercise capacity in rodents^{10,13,17,18}. Administration of S107 (via a subcutaneous infusion pump to achieve a plasma level of 252 ± 75.1 nM; s.e.m., $n = 10$) improved forelimb grip strength and *ex vivo* muscle-specific force of the EDL in mice with breast cancer-associated bone metastases as compared to vehicle-treated mice (**Fig. 2a,b**). S107 prevented depletion of calstabin1 from the skeletal muscle RyR1 complex in mice with bone metastases but, as previously reported, did not prevent oxidation or nitrosylation of RyR1 (refs. 10,13) (**Fig. 2c**). S107 treatment led to higher peak tetanic Ca^{2+} in muscle fibers (**Fig. 2d**) and lower skeletal muscle RyR1 open probability (P_o) (**Fig. 2e**), consistent with decreased SR Ca^{2+} leak, than in vehicle-treated mice. The SR/ER Ca^{2+} ATPase (SERCA) pumps Ca^{2+} back into the SR, and lower SERCA activity could contribute to decreased tetanic Ca^{2+} ; however, we observed no difference in SERCA activity in skeletal muscle from non-tumor mice as compared to that from mice with bone metastases (either with or without S107 treatment) (**Fig. 2f**).

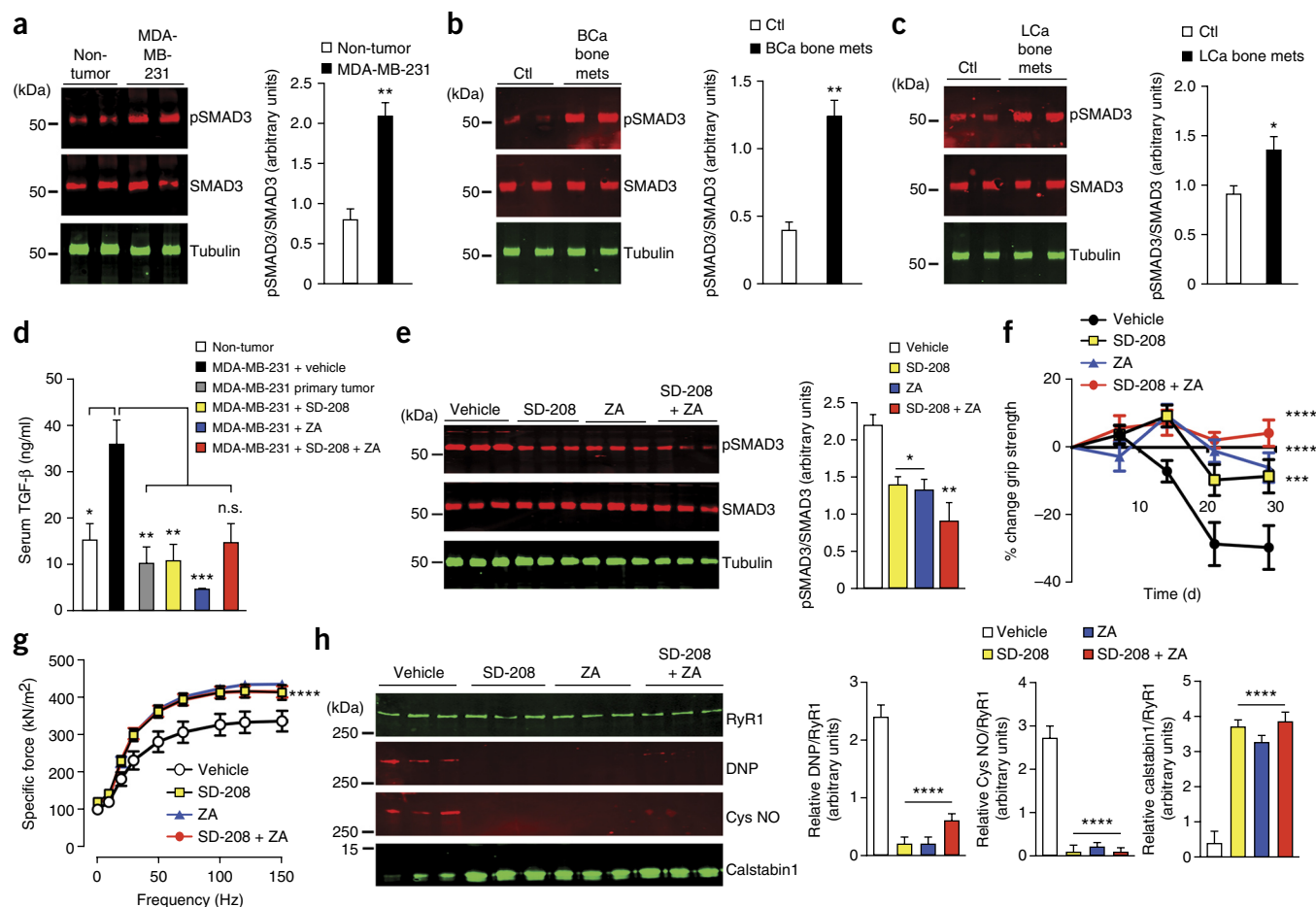


Figure 3 Blocking TGF- β signaling or inhibiting bone resorption lowers SMAD3 phosphorylation and improves muscle function. (**a–c**) Immunoblots of SMAD3 phosphorylation (left) and quantification (right) from muscle of mice with MDA-MB-231 bone metastases (**a**) and from muscle samples of humans with either breast cancer (BCa bone mets) (**b**) or lung cancer bone metastases (LCa bone mets) (**c**) and their respective controls (Ctl); $n = 4$ per group. (**d**) Serum TGF- β concentration in non-tumor control mice, mice with MDA-MB-231 bone metastases, mice with MDA-MB-231 primary tumors or mice with MDA-MB-231 bone metastases receiving treatment to block TGF- β signaling (SD-208) or bone resorption (zoledronic acid (ZA)) ($n = 5$). (**e**) SMAD3 phosphorylation in mice with MDA-MB-231 bone metastases receiving either SD-208, ZA or combined therapy ($n = 3$). (**f,g**) *In vivo* forelimb grip strength ($n = 12$ per group) (**f**) and *ex vivo* specific force of the EDL muscle ($n = 12$ per group) (**g**) in mice treated with SD-208, ZA or a combination of both. (**h**) Immunoblot (left) and quantification (right) of RyR1 oxidation (DNP) and nitrosylation (Cys NO) and of RyR1-calstabin1 binding, as measured by coimmunoprecipitation, from EDL muscle ($n = 3$ per group). Data are mean \pm s.e.m. Statistical analysis in **a–c** was by Student's *t*-test, in **d,e,h** was by one-way ANOVA with multiple comparisons and in **f,g** was by two-way ANOVA. * $P < 0.05$, ** $P < 0.01$, *** $P < 0.001$, **** $P < 0.0001$; n.s., not significant.

S107 treatment had no effect on the development and progression of bone metastases, tumor burden, the number of osteoclasts present at the tumor bone interface (**Supplementary Fig. 4a**), body weight, or the distribution of fat and lean mass as compared to what we observed in vehicle-treated mice (**Supplementary Fig. 4b**). S107 treatment did not improve muscle mass or affect muscle fiber diameter or mid-calf cross-sectional area (**Supplementary Fig. 4c**). However, S107 treatment did eliminate the correlation between higher bone destruction and lower muscle function (**Fig. 2g**).

Calorie restriction, by reducing food intake (**Supplementary Fig. 4d**) in healthy mice for 2 weeks, led to reduced body weight and fat and lean mass, and led to lower muscle weight and reduced mid-calf cross-sectional area as compared to pair-fed mice (**Supplementary Fig. 4e**). Grip strength and *ex vivo* contractility of the EDL muscle were not affected by reduced calorie intake (**Supplementary Fig. 4f**). This shows that loss of muscle mass alone does not account for lower strength in mice with bone metastases.

Inhibiting TGF- β improves muscle strength

Bone is the largest source of TGF- β in the body¹⁹, and TGF- β (which is deposited in bone matrix by osteoblasts) has a central role in tumor growth in bone^{6,7,20,21}. TGF- β is released from mineralized bone matrix during osteoclastic resorption. This resorbing bone matrix is the primary source of TGF- β activity in mice with MDA-MB-231 bone metastases; bisphosphonate inhibition of osteoclastic bone resorption therefore effectively inhibits excess TGF- β signaling in these bone metastases^{7,19}. We found that TGF- β -induced phosphorylation of the signaling factor SMAD3 (ref. 22) was higher in skeletal muscle from mice with MDA-MB-231 breast cancer bone metastases than in non-tumor control mice (**Fig. 3a**) but not in mice with MDA-MB-231 primary tumors without bone metastases (**Supplementary Fig. 5a**), consistent with a systemic effect of bone-derived TGF- β on skeletal muscle. The clinical relevance of the activation of TGF- β -mediated signaling in skeletal muscle in the presence of cancer-induced bone destruction was reinforced because SMAD3 phosphorylation was also

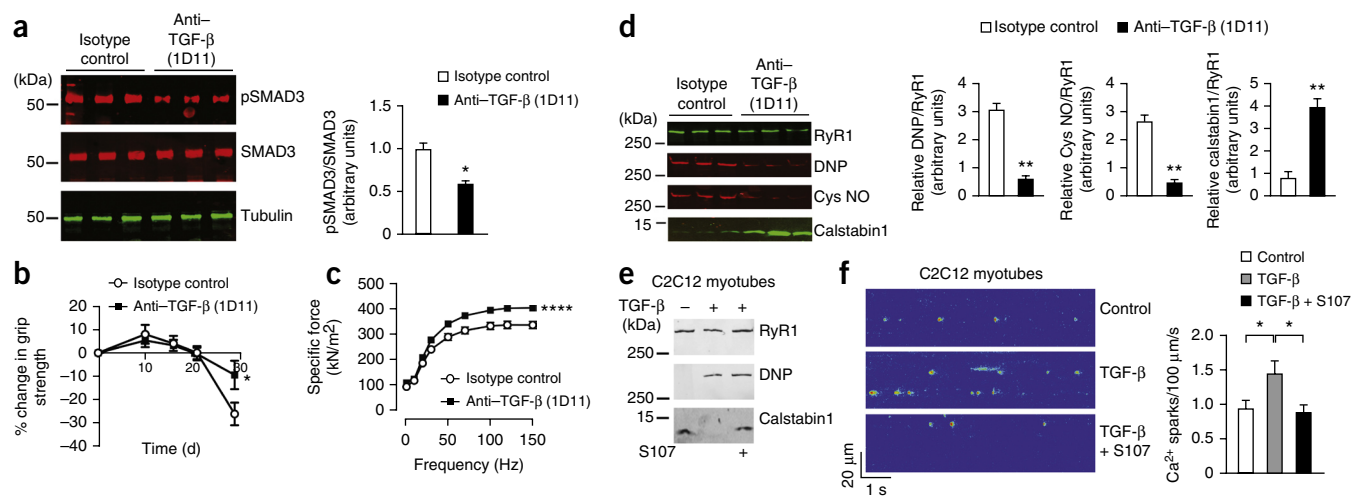


Figure 4 Blocking TGF- β ligand lowers SMAD3 phosphorylation and improves muscle function. (a) Immunoblot (left) and quantification (right) of SMAD3 phosphorylation in muscle from mice with MDA-MB-231 bone metastases receiving 1D11 treatment ($n = 3$). (b,c) *In vivo* forelimb grip strength (b) and *ex vivo* specific force of the EDL muscle (c) in mice treated with a TGF- β neutralizing antibody (clone 1D11) ($n = 11$ per group). (d) Immunoblot (left) and quantification (right) of RyR1 oxidation (DNP) and nitrosylation (Cys NO) and of RyR1-calstabin1 binding, as measured by coimmunoprecipitation, from EDL muscle ($n = 3$). (e) Immunoblot analysis of RyR1 oxidation and of RyR1-calstabin1 binding, as measured by coimmunoprecipitation, in C2C12 cells treated with TGF- β \pm S107. (f) Ca²⁺ sparks in C2C12 myotubes treated with TGF- β \pm S107 ($n = 52$ cells). Data are mean \pm s.e.m. Statistical analysis in a,d was by Student's *t*-test, in b,c was by two-way ANOVA and in f was by one-way ANOVA with multiple comparisons. * $P < 0.05$, ** $P < 0.01$, **** $P < 0.0001$.

higher in skeletal muscle from humans with breast cancer bone metastases (Fig. 3b) and in humans with lung cancer bone metastases than in skeletal muscle from humans without bone metastases (Fig. 3c). Serum TGF- β concentrations were higher in tumor-bearing mice with bone metastases, but not in those with primary breast cancer compared to non-tumor mice (Fig. 3d). Skeletal muscle from five additional mouse models of human cancers with osteolytic or mixed osteolytic/osteoblastic bone metastases due to A549 lung cancer, RWGT2 lung cancer, MCF-7 breast cancer, PC-3 prostate cancer, and JFN-3 multiple myeloma all showed higher SMAD3 phosphorylation, consistent with activation of TGF- β -mediated signaling in skeletal muscle compared to non-tumor control mice (Supplementary Fig. 5a). In contrast, the osteoblastic ZR75-1 breast cancer bone metastases did not exhibit higher SMAD3 phosphorylation in skeletal muscle compared to non-tumor control mice (Supplementary Fig. 5a).

Next we showed that inhibition of TGF- β improves muscle strength. We treated mice with MDA-MB-231 bone metastases with: (i) the TGF- β receptor I kinase inhibitor SD-208 (60 mg per kg body weight daily gavage); (ii) the bisphosphonate zoledronic acid (ZA) (5 μ g per kg body weight; three treatments per week by subcutaneous injection), which specifically inhibits osteoclastic bone resorption and lowers TGF- β release from the bone matrix⁷; (iii) combined therapy (SD-208 + ZA); or (iv) a pan-TGF- β neutralizing antibody (clone 1D11)²³. Serum TGF- β concentrations were decreased in MDA-MB-231 tumor-bearing mice with bone metastases treated with ZA as a consequence of lower release of TGF- β from the bone than in vehicle-treated mice (Fig. 3d). Bone metastases-bearing mice treated with SD-208, ZA or the combination of both, all had lower levels of skeletal muscle SMAD3 phosphorylation than observed for SMAD3 in vehicle-treated mice, indicating inhibition of TGF- β signaling (Fig. 3e). Both SD-208 and ZA treatment, alone and in combination, improved muscle function (forelimb grip strength and muscle-specific force of the EDL) (Fig. 3f,g) and RyR1 oxidation and nitrosylation and preserved calstabin1 binding to the RyR1 complex (Fig. 3h). The activity of SERCA was not affected by treatment with

SD-208, ZA, or combined therapy compared to vehicle-treated mice (Supplementary Fig. 5b). *In vitro*, SD-208 blocked TGF- β -induced SMAD3 phosphorylation in C2C12 myotubes, a mouse myoblast cell line used for the *in vitro* study of skeletal muscle (Supplementary Fig. 5c). Taken together, these data show that bone-derived TGF- β has a key role in reduced muscle-specific force production and in cancer-associated muscle weakness, possibly via oxidation of RyR1.

SD-208 or ZA treatment prevented loss of skeletal muscle, body weight and lower mid-calf cross-sectional area in mice with bone metastases, and the combined therapy (SD-208 + ZA) provided an additive benefit (Supplementary Fig. 5d-g), a lower tumor burden (Supplementary Fig. 5h) and a lower number of osteoclasts at the tumor-bone interface compared to vehicle-treated mice (Supplementary Fig. 5i).

Because SD-208 is a TGF- β receptor I kinase inhibitor, it may also inhibit the effects of other TGF- β family members, including activin and myostatin. To determine the specificity of TGF- β to induce muscle weakness we treated mice with breast cancer bone metastases with a pan-TGF- β neutralizing antibody (clone 1D11)²³ or isotype control (10 mg per kg body weight (mg/kg), three times per week by intraperitoneal injection)²⁴. The TGF- β -neutralizing 1D11 antibody has no effect on activin or myostatin signaling²³. Mice with MDA-MB-231 breast cancer bone metastases treated with the 1D11 antibody showed decreased SMAD3 phosphorylation (Fig. 4a), increased forelimb grip strength and *ex vivo* specific force generation of the EDL muscle (Fig. 4b,c), reduced RyR1 oxidation and nitrosylation and increased binding of calstabin1 to the RyR1 complex, consistent with fixing of the leaky RyR1 channels, than in isotype antibody-treated control mice (Fig. 4d). 1D11 treatment lowered SMAD3 phosphorylation in TGF- β -treated C2C12 myotubes, as compared to that observed in isotype antibody control-treated cells (Supplementary Fig. 6a). 1D11-treated mice showed increased hindlimb muscle weight, increased body weight (due to increases in both fat and lean content) and greater mid-calf cross-sectional area than in isotype antibody-treated control mice (Supplementary Fig. 6b-e). Mice treated with 1D11 had lower bone

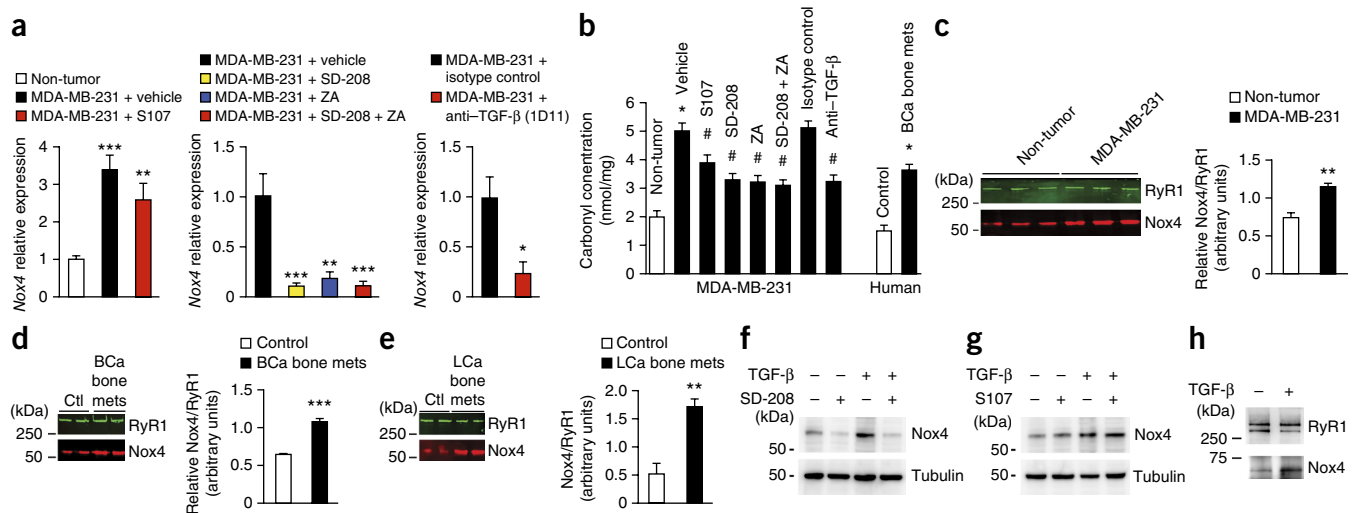


Figure 5 TGF- β activity leads to higher NADPH oxidase 4 (Nox4) expression and RyR1-Nox4 interaction. (a) Nox4 mRNA expression in the tibialis anterior (TA) muscle of mice with MDA-MB-231 breast cancer bone metastases treated with S107 (left), SD-208 and/or zoledronic acid (middle) or TGF- β -specific 1D11 antibody (right) ($n = 3$ per group). (b) Protein carbonyl concentration in muscle from either mice with MDA-MB-231 bone metastases or humans with breast cancer and bone metastases ($n = 2$ for each group). Data are mean \pm s.d. Statistical analysis was by two-way ANOVA; * $P < 0.05$ as compared to non-tumor control mice or human control samples; # $P < 0.05$ as compared to vehicle-treated controls. (c–e) Immunoblot (left) and quantification (right) of Nox4 coimmunoprecipitation with RyR1 in muscle from mice with MDA-MB-231 bone metastases (c) ($n = 3$), muscle samples from humans with breast cancer and bone metastases (BCa bone mets) (d) ($n = 4$) and muscle samples from humans with lung cancer and bone metastases (LCa bone mets) (e) ($n = 4$) and their respective controls (in c, $n = 3$; in d, e, $n = 4$). (f, g) Immunoblot of Nox4 expression in C2C12 myotubes treated with either TGF- β \pm SD-208 (f) or TGF- β \pm S107 (g). (h) Immunoblot showing Nox4 coimmunoprecipitation with RyR1 in C2C12 myotubes treated with TGF- β . (i) Immunoblots of C2C12 cells showing either knockdown of Nox4 using a Nox4-specific shRNA (left; shNox4 versus scrambled control shScr) or RyR1 oxidation (DNP) and RyR1-calstabin1 binding, as measured by co-immunoprecipitation (right). C2C12 myotubes were either untreated or treated with TGF- β . (j) Relative ROS generation in C2C12 myotubes ($n = 4$). H₂O₂, hydrogen peroxide. Data are mean \pm s.e.m. Statistical analysis in a, b, j was by one-way ANOVA with multiple comparisons and in c–e was by Student's *t*-test. * $P < 0.05$, ** $P < 0.01$, *** $P < 0.001$, **** $P < 0.0001$.

destruction (osteolytic lesion area of limbs) (Supplementary Fig. 6f, g) and lower tumor burden, and we observed no effect on the number of osteoclasts at the tumor-bone interface as compared to isotype antibody-treated control mice (Supplementary Fig. 6h, i). Taken together, these data indicate that TGF- β inhibition improves muscle function and that bone-derived TGF- β contributes to cancer-associated muscle weakness, at least in part, by inducing oxidation of RyR1.

To directly show that TGF- β is sufficient to cause RyR1 channel remodeling and intracellular Ca²⁺ leakage, we treated differentiated C2C12 myotubes with TGF- β , which induced the biochemical signature of leaky RyR1. Binding of calstabin1 to RyR1 (which fixes the RyR1-mediated leak) was restored by incubation of myotubes with S107 compared to C2C12 myotubes without TGF- β treatment (Fig. 4e). TGF- β treatment increased Ca²⁺ sparks in myotubes (a direct measure of RyR1-mediated SR Ca²⁺ leakage), as compared to those in C2C12 myotubes without TGF- β treatment, and the increase in the number of Ca²⁺ sparks was prevented by treatment with S107 (Fig. 4f). Thus, TGF- β activates a signaling pathway that leads to RyR1 oxidation and to SR Ca²⁺ leakage in skeletal muscle cells.

RyR1 oxidation is mediated by Nox4

We next sought to determine the mechanisms by which TGF- β mediates oxidation of RyR1. Nox4 is a membrane protein that transfers electrons from NADPH to oxygen (O₂) to form reactive oxygen

species (ROS), which oxidize many molecules including proteins. Nox4 is expressed in skeletal muscles, including in the SR where it interacts with RyR1, resulting in its oxidation²⁵. TGF- β treatment leads to higher expression of Nox4 (refs. 26–29). We found that skeletal muscle from mice with bone metastases had threefold higher Nox4 mRNA levels than in non-tumor control mice, and S107 treatment had no effect on Nox4 expression (Fig. 5a). Treatment with SD-208, ZA, SD-208 + ZA or 1D11 antibody lowered skeletal muscle Nox4 mRNA expression as compared to that in appropriate vehicle-treated control mice (Fig. 5a). Nox1 and Nox2 mRNA were not altered in mice with MDA-MB-231 bone metastases as compared to non-tumor control mice (Supplementary Fig. 7a). Moreover, total protein oxidation (measured as carbonyl concentration in skeletal muscle lysates, as described in the Online Methods) was higher in skeletal muscle from mice and humans with cancer and bone metastases as compared to that from mice and humans without bone metastases. Inhibition of TGF- β signaling decreased protein oxidation in the mice with bone metastases as compared to that in vehicle-treated mice (Fig. 5b). Indeed, total protein oxidation (carbonyl concentration) was higher in skeletal muscle from all bone metastasis models associated with bone destruction, but not in skeletal muscle from mice with primary MDA-MB-231 breast cancer without bone metastases, or in those with osteoblastic ZR75-1 bone metastases as compared to non-tumor control mice. These data indicate that tumor-induced bone

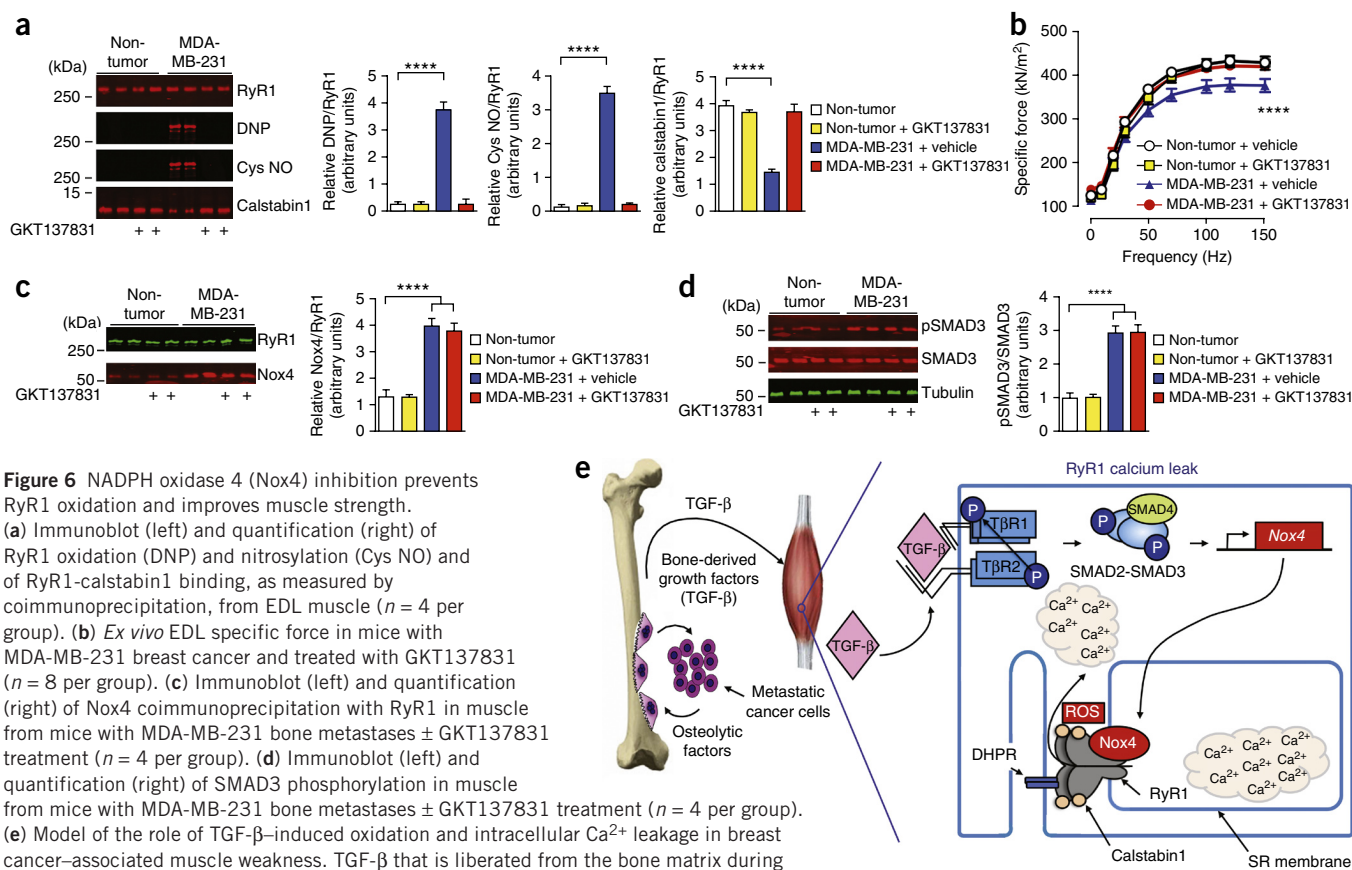


Figure 6 NADPH oxidase 4 (Nox4) inhibition prevents RyR1 oxidation and improves muscle strength. (a) Immunoblot (left) and quantification (right) of RyR1 oxidation (DNP) and nitrosylation (Cys NO) and of RyR1-calstabin1 binding, as measured by coimmunoprecipitation, from EDL muscle ($n = 4$ per group). (b) *Ex vivo* EDL specific force in mice with MDA-MB-231 breast cancer and treated with GKT137831 ($n = 8$ per group). (c) Immunoblot (left) and quantification (right) of Nox4 coimmunoprecipitation with RyR1 in muscle from mice with MDA-MB-231 bone metastases \pm GKT137831 treatment ($n = 4$ per group). (d) Immunoblot (left) and quantification (right) of SMAD3 phosphorylation in muscle from mice with MDA-MB-231 bone metastases \pm GKT137831 treatment ($n = 4$ per group). (e) Model of the role of TGF- β -induced oxidation and intracellular Ca²⁺ leakage in breast cancer-associated muscle weakness. TGF- β that is liberated from the bone matrix during osteolytic bone destruction drives the expression of Nox4 in muscle via SMAD2-SMAD3 signaling, and Nox4 activity produces ROS. Oxidation of RyR1 leads to loss of calstabin1 binding and Ca²⁺ leakage from the sarcoplasmic reticulum, thereby depleting intracellular Ca²⁺ stores and causing decreased muscle-specific force. Inhibiting TGF- β release from the bone matrix, TGF- β signaling, Nox4 activity or RyR1-mediated SR Ca²⁺ leakage improved muscle strength. DHPR, dihydropyridine receptor; T β R1, TGF- β receptor 1; T β R2, TGF- β receptor 2. Data are mean \pm s.e.m. Statistical analysis in **a,c,d** was by one-way ANOVA with multiple comparisons and in **b** was by two-way ANOVA. **** $P < 0.0001$.

destruction is associated with oxidation of skeletal muscle. Moreover, inhibiting TGF- β release, or signaling, or blocking Nox4 lowered the carbonyl concentration in skeletal muscle lysates from mice with tumors metastatic to bone (Supplementary Table 3), indicating the importance of TGF- β and Nox4 in the oxidation of skeletal muscle proteins in the setting of tumors metastatic to bone.

Nox4 coimmunoprecipitated with RyR1 specifically from skeletal muscle from mice with MDA-MB-231 breast cancer bone metastases (Fig. 5c) and from skeletal muscle samples from humans with breast cancer bone metastases or humans with lung cancer bone metastases (Fig. 5d,e). The amount of Nox4 that coimmunoprecipitated with RyR1 was higher in muscles from mice with breast cancer bone metastases (Fig. 5c and Supplementary Fig. 7b), from humans with breast cancer bone metastases (Fig. 5d), from mice with lung cancer bone metastases (Supplementary Fig. 7b), from humans with lung cancer bone metastases (Fig. 5e), from mice with PC-3 prostate cancer and from mice with JJN-3 multiple myeloma as compared to that in non-tumor controls. Skeletal muscle from mice with MDA-MB-231 primary breast cancer without bone metastases or mice with ZR75-1 osteoblastic breast cancer bone metastases that were not associated with RyR1 oxidation did not show RyR1 and Nox4 coimmunoprecipitation greater than that observed in non-tumor control mice (Supplementary Fig. 7b).

TGF- β treatment resulted in higher Nox4 protein expression in C2C12 myotubes as compared to that in C2C12 myotubes without TGF- β treatment, and this was blocked by treatment with SD-208,

but not S107 (Fig. 5f,g). TGF- β treatment led to increased coimmunoprecipitation of Nox4 with RyR1 channels in myotubes (Fig. 5h). Moreover, Nox4 knockdown in myotubes prevented TGF- β -induced RyR1 oxidation and loss of calstabin1 binding to RyR1 (Fig. 5i) and prevented TGF- β -induced ROS production compared to that observed in C2C12 myotubes without TGF- β treatment (Fig. 5j).

To test the *in vivo* effect of Nox4 inhibition, we treated mice with MDA-MB-231 breast cancer bone metastases with the Nox1 and Nox4 inhibitor GKT137831 (ref. 30) (60 mg/kg/d or vehicle (1.2% methylcellulose + 0.1% polysorbate 80), administered by daily oral gavage). GKT137831 treatment prevented skeletal muscle oxidation and nitrosylation of RyR1, restored calstabin1 binding (Fig. 6a) and improved EDL muscle-specific force (Fig. 6b). GKT137831 had no effect on the amount of skeletal muscle Nox4 associated with RyR1 (Fig. 6c), and it did not block upstream TGF- β signaling, as skeletal muscle SMAD3 phosphorylation was not affected in comparison to that in vehicle-treated mice (Fig. 6d). In mice with bone metastases, GKT137831 had no effect on osteolytic lesion size, muscle mass, body weight, body composition or grip strength, probably reflecting the high variability of the latter measurement, which also has a behavioral component (Supplementary Fig. 7c-h).

No contribution by non-bone sites or fibrosis to weakness

The tumor-bone microenvironment appears to be the most significant determinant of muscle weakness in this model, as the bisphosphonate

zoledronic acid prevented oxidation of RyR1 and muscle weakness by blocking release of TGF- β from bone. Consistent with this, tumor burden at other metastatic sites was insignificant. In mice with MDA-MB-231 breast cancer and bone metastases, the tumor burden in bone was at least 12-fold higher than in all other organs (**Supplementary Fig. 8a**). Further, there was no evidence of skeletal muscle fibrosis (**Supplementary Fig. 8b**), supporting the finding that muscle weakness is due to tumor-induced bone destruction.

To validate the role that higher bone resorption has in skeletal muscle weakness in the absence of cancer, we tested a mouse model of CED. This disease is an inherited human skeletal disease characterized by increased bone destruction and skeletal fragility and is often associated with TGF- β 1 mutations that cause an increase in TGF- β activity by increased activation or secretion of TGF- β (refs. 31,32). In the mouse model of CED, a mutant TGF- β 1 (H222D), identified from some humans with CED, is expressed under the control of the 2.3-kb type I collagen promoter. These mice show higher bone destruction and fractures that is abrogated by TGF- β signaling blockade using a TGF- β receptor I inhibitor. CED mice show higher concentrations of active TGF- β in the bone microenvironment and higher bone resorption as compared to littermate controls⁸. Radiography of the lower hindlimb of CED mice showed osteolysis and diaphyseal dysplasia, similarly to that observed in previous reports, as compared to littermate controls⁸ (**Supplementary Fig. 8c**). Consistent with higher TGF- β signaling, skeletal muscle from CED mice had higher SMAD3 phosphorylation than that of littermate control mice (**Supplementary Fig. 8d**). CED mice also had lower *ex vivo* specific force of the EDL muscle as compared to that in non-affected littermate control mice (**Supplementary Fig. 8e**), consistent with previous reports in which treatment of mice with recombinant TGF- β resulted in lower skeletal muscle-specific force³³. Skeletal muscle from CED mice also showed higher levels of RyR1 oxidation and nitrosylation, lower amounts of calstabin1 bound to RyR1 and higher levels of Nox4-RyR1 binding as compared to those in littermate control mice (**Supplementary Fig. 8f**). These results were similar to those we observed in mice with osteolytic bone metastases.

Taken together, our data in models of osteolytic bone metastases show that TGF- β , released from the bone matrix due to elevated catabolism of the tissue, upregulates *Nox4* and causes higher association of Nox4 protein with RyR1, resulting in oxidation of the channel. RyR1 oxidation causes an SR Ca²⁺ leak that lowers tetanic Ca²⁺, impairs muscle force production and contributes to muscle weakness in cancer with bone metastases (**Fig. 6e**). Similar skeletal muscle dysfunction, higher skeletal muscle TGF- β activity and RyR1 oxidation via upregulation of Nox4 were observed in a nonmalignant bone disorder associated with increased bone destruction (CED mice).

DISCUSSION

The present study provides novel mechanistic insights into the causes of cancer-associated muscle weakness with potential therapeutic implications for the following reasons: (i) in addition to loss of muscle mass, we now show that there is a specific loss of muscle function in the setting of bone metastases and that muscle weakness can occur without the loss of muscle mass; (ii) an important determinant of muscle weakness in metastatic cancer is bone destruction; (iii) a key mediator of muscle weakness is TGF- β that is released from bone as a consequence of tumor-induced osteoclast activity in the tumor-bone microenvironment; (iv) TGF- β activates Nox4 in skeletal muscle, causing protein oxidation; (v) skeletal muscle RyR1 Ca²⁺-release channels are a target of the oxidative stress that

results from the upregulation of Nox4 by TGF- β ; (vi) RyR1 oxidation results in intracellular Ca²⁺ leakage that lowers tetanic Ca²⁺ and weakens muscle force production; (vii) activation of TGF- β signaling, upregulation of Nox4 and the biochemical signature of oxidation-induced skeletal muscle RyR1 leakage were present in humans with breast or lung cancer metastatic to bone and in six out of seven mouse models of human osteolytic bone metastases, including those of breast, lung and prostate cancers, as well as that of multiple myeloma; and (viii) inhibition of RyR1-mediated SR Ca²⁺ leakage, inhibition of TGF- β activity, inhibition of TGF- β release from bone or inhibition of Nox4 improved muscle force production, suggesting that these processes could be potential therapeutic targets for cancer-associated muscle weakness in the setting of bone destruction due to metastases. Furthermore, this mechanism of muscle weakness was also observed in a nonmalignant bone disorder that is characterized by increased bone destruction and TGF- β activity. Thus, targeting skeletal muscle weakness caused by the TGF- β -Nox4-RyR1 axis represents a novel therapeutic approach to improving the quality of life in cancer patients with muscle weakness associated with increased bone destruction.

In addition to RyR1, other proteins involved in muscle contraction were oxidized in skeletal muscle from mice with bone metastases, suggesting that there may be other contributing factors to cancer-associated muscle weakness. Inhibition of the activin receptor reduces cachexia and cardiac atrophy and improves survival in mice with experimental colon cancer cachexia (C26 model)³⁴. Another target under investigation for cachexia is myostatin, a negative regulator of muscle mass³⁵. Myostatin antagonism with a myostatin-specific antibody improves the contractile properties of dystrophic muscle in the *mdx* mouse model of Duchenne muscular dystrophy³⁶. However, myostatin-deficient mice show a decrease in muscle contractile force that is age, sex and muscle dependent^{2,3}. Our data do not exclude the possibility that other bone-derived factor(s) released as a consequence of osteoclastic bone resorption may induce TGF- β production from other sources or that they may themselves contribute to skeletal muscle dysfunction or loss of muscle mass. Furthermore, the data do not indicate that the mechanism described herein is the exclusive one for cancer-associated muscle weakness but rather suggests that this is one such mechanism that may be operational in humans with bone metastases.

Taken together, our data provide a link between bone and skeletal muscle by showing that factors elaborated from bone can profoundly affect muscle function systemically. Our findings in mouse models of breast cancer, lung cancer, prostate cancer and multiple myeloma, and in humans with breast cancer or lung cancer that is associated with bone destruction, suggest a generalized but not exclusive role for the tumor-bone microenvironment in the generation of cancer-associated skeletal muscle weakness. Finally, the data indicate that muscle dysfunction can occur before the loss of muscle mass (cachexia) and suggest that a spectrum of muscle dysfunction, ranging from muscle weakness to profound cachexia, exists in humans with bone metastases. Indeed, muscle weakness may occur in states of increased bone destruction, even in the absence of cancer. Clinical studies to characterize this spectrum of muscle dysfunction are justified to allow for the development and testing of treatments to ameliorate the muscle weakness that is associated with cancer and associated bone disorders.

METHODS

Methods and any associated references are available in the [online version of the paper](#).

Note: Any Supplementary Information and Source Data files are available in the online version of the paper.

ACKNOWLEDGMENTS

This work was supported by the US National Institutes of Health (NIH) (grant U01CA143057 (T.A.G.) from the National Cancer Institute (NCI) Tumor Microenvironment Network, NCI-R01CA69158 (T.A.G.), NCI-R21CA179017 (G.D.R.), NHLBI-R01HL061503 (A.R.M.), NHLBI-R01HL102040 (A.R.M.), NIAMS-R01AR060037 (A.R.M.), NIH T32 HL120826 (A.R.M.), NINDS-R25NS076445 (A.R.M.), NIH-NINDS R25NS076445 (A.H.), NIH-NIAMS R01AR063943 (X.C.), and NIH-NHLBI T35 HL110854-01 (S.C. and P.K.), the Susan G. Komen Foundation (grant SAC110013; T.A.G.), the Indiana Economic Development Grant (T.A.G.), the Jerry and Peggy Throgmartin Endowment of the Indiana University Simon Cancer Center (T.A.G.), the Indiana University Simon Cancer Center Breast Cancer Program (T.A.G.), the American Cancer Society and Indiana University Simon Cancer Center (grant IRG-84-002-28; D.L.W.), the Indiana University Health Strategic Research Initiative in Oncology (D.L.W.), the VA Merit Review Award (G.D.R.), the Fondation Leducq (A.R.M.), the Ellison Foundation (A.R.M.), the Swedish Heart Lung Foundation and Stockholm County Council (D.C.A.) and a generous donation from the Withycombe family (T.A.G.). Camurati-Engelmann disease (CED) mice were previously described and provided by X. Cao (Johns Hopkins, Baltimore, MD).

AUTHOR CONTRIBUTIONS

All contributing authors have agreed to submission of this manuscript for publication. T.A.G. and A.R.M. conceived of the study. D.L.W., K.S.M., A.R.M. and T.A.G. designed and performed experiments, analyzed data and interpreted results. S.R., W.X., D.C.A., S.J., M.N., A.C., L.E.W., A.W., A.H., A.U., T.T., S.C., F.A.W. and P.K. performed experiments. M.S.B. analyzed data. G.D.R. and F.A.W. designed experiments and interpreted results. G.Z., X.W. and X.C. provided the CED mice and reviewed the results. D.L.W., K.S.M., A.R.M. and T.A.G. wrote the manuscript.

COMPETING FINANCIAL INTERESTS

The authors declare competing financial interests: details are available in the online version of the paper.

Reprints and permissions information is available online at <http://www.nature.com/reprints/index.html>.

1. Fearon, K.C., Glass, D.J. & Guttridge, D.C. Cancer cachexia: mediators, signaling and metabolic pathways. *Cell Metab.* **16**, 153–166 (2012).
2. Gentry, B.A., Ferreira, J.A., Phillips, C.L. & Brown, M. Hindlimb skeletal muscle function in myostatin-deficient mice. *Muscle Nerve* **43**, 49–57 (2011).
3. Mendias, C.L., Marcin, J.E., Calderon, D.R. & Faulkner, J.A. Contractile properties of EDL and soleus muscles of myostatin-deficient mice. *J. Appl. Physiol.* **101**, 898–905 (2006).
4. Weilbaecher, K.N., Guise, T.A. & McCauley, L.K. Cancer to bone: a fatal attraction. *Nat. Rev. Cancer* **11**, 411–425 (2011).
5. Coleman, R.E. *et al.* Metastasis and bone loss: advancing treatment and prevention. *Cancer Treat. Rev.* **36**, 615–620 (2010).
6. Kang, Y. *et al.* Breast cancer bone metastasis mediated by the Smad tumor suppressor pathway. *Proc. Natl. Acad. Sci. USA* **102**, 13909–13914 (2005).
7. Korpai, M. *et al.* Imaging transforming growth factor- β signaling dynamics and therapeutic response in breast cancer bone metastasis. *Nat. Med.* **15**, 960–966 (2009).
8. Tang, Y. *et al.* TGF- β 1-induced migration of bone mesenchymal stem cells couples bone resorption with formation. *Nat. Med.* **15**, 757–765 (2009).
9. Zalk, R., Lehnart, S.E. & Marks, A.R. Modulation of the ryanodine receptor and intracellular calcium. *Annu. Rev. Biochem.* **76**, 367–385 (2007).
10. Andersson, D.C. *et al.* Ryanodine receptor oxidation causes intracellular calcium leak and muscle weakness in aging. *Cell Metab.* **14**, 196–207 (2011).
11. Guise, T.A. *et al.* Evidence for a causal role of parathyroid hormone-related protein in the pathogenesis of human breast cancer-mediated osteolysis. *J. Clin. Invest.* **98**, 1544–1549 (1996).
12. Vera-Ramirez, L. *et al.* Free radicals in breast carcinogenesis, breast cancer progression and cancer stem cells. Biological bases to develop oxidative-based therapies. *Crit. Rev. Oncol. Hematol.* **80**, 347–368 (2011).
13. Bellinger, A.M. *et al.* Hypernitrosylated ryanodine receptor calcium release channels are leaky in dystrophic muscle. *Nat. Med.* **15**, 325–330 (2009).
14. Lu, X. & Kang, Y. Efficient acquisition of dual metastasis organotropism to bone and lung through stable spontaneous fusion between MDA-MB-231 variants. *Proc. Natl. Acad. Sci. USA* **106**, 9385–9390 (2009).
15. Guise, T.A., Yoneda, T., Yates, A.J. & Mundy, G.R. The combined effect of tumor-produced parathyroid hormone-related protein and transforming growth factor- α enhance hypercalcemia *in vivo* and bone resorption *in vitro*. *J. Clin. Endocrinol. Metab.* **77**, 40–45 (1993).
16. Hjorth-Hansen, H. *et al.* Marked osteoblastopenia and reduced bone formation in a model of multiple myeloma bone disease in severe combined immunodeficiency mice. *J. Bone Miner. Res.* **14**, 256–263 (1999).
17. Bellinger, A.M. *et al.* Remodeling of ryanodine receptor complex causes 'leaky' channels: a molecular mechanism for decreased exercise capacity. *Proc. Natl. Acad. Sci. USA* **105**, 2198–2202 (2008).
18. Andersson, D.C. & Marks, A.R. Fixing ryanodine receptor Ca leak: a novel therapeutic strategy for contractile failure in heart and skeletal muscle. *Drug Discov. Today Dis. Mech.* **7**, e151–e157 (2010).
19. Dallas, S.L., Rosser, J.L., Mundy, G.R. & Bonewald, L.F. Proteolysis of latent transforming growth factor- β (TGF- β)-binding protein-1 by osteoclasts. A cellular mechanism for release of TGF- β from bone matrix. *J. Biol. Chem.* **277**, 21352–21360 (2002).
20. Kang, Y. *et al.* A multigenic program mediating breast cancer metastasis to bone. *Cancer Cell* **3**, 537–549 (2003).
21. Yin, J.J. *et al.* TGF- β signaling blockade inhibits PTHrP secretion by breast cancer cells and bone metastases development. *J. Clin. Invest.* **103**, 197–206 (1999).
22. Shi, Y. & Massagué, J. Mechanisms of TGF- β signaling from cell membrane to the nucleus. *Cell* **113**, 685–700 (2003).
23. Dasch, J.R., Pace, D.R., Waegell, W., Inenaga, D. & Ellingsworth, L. Monoclonal antibodies recognizing transforming growth factor- β . Bioactivity neutralization and transforming growth factor β 2 affinity purification. *J. Immunol.* **142**, 1536–1541 (1989).
24. Biswas, S. *et al.* Anti-transforming growth factor α antibody treatment rescues bone loss and prevents breast cancer metastasis to bone. *PLoS ONE* **6**, e27090 (2011).
25. Sun, Q.A. *et al.* Oxygen-coupled redox regulation of the skeletal muscle ryanodine receptor-Ca²⁺ release channel by NADPH oxidase 4. *Proc. Natl. Acad. Sci. USA* **108**, 16098–16103 (2011).
26. Carmona-Cuenca, I. *et al.* Upregulation of the NADPH oxidase NOX4 by TGF- β in hepatocytes is required for its pro-apoptotic activity. *J. Hepatol.* **49**, 965–976 (2008).
27. Hubackova, S., Krejčíková, K., Bartek, J. & Hodny, Z. IL-1 and TGF- β -Nox4 signaling, oxidative stress and DNA damage response are shared features of replicative, oncogene-induced and drug-induced paracrine 'bystander senescence'. *Aging (Albany NY)* **4**, 932–951 (2012).
28. Michaeloudes, C., Sukkar, M.B., Khorasani, N.M., Bhavsar, P.K. & Chung, K.F. TGF- β regulates Nox4, MnSOD and catalase expression and IL-6 release in airway smooth muscle cells. *Am. J. Physiol. Lung Cell. Mol. Physiol.* **300**, L295–L304 (2011).
29. Yan, F. *et al.* Nox4 and redox signaling mediate TGF- β -induced endothelial cell apoptosis and phenotypic switch. *Cell Death Dis.* **5**, e1010 (2014).
30. Jiang, J.X. *et al.* Liver fibrosis and hepatocyte apoptosis are attenuated by GKT137831, a novel NOX4/NOX1 inhibitor *in vivo*. *Free Radic. Biol. Med.* **53**, 289–296 (2012).
31. Janssens, K. *et al.* Mutations in the gene encoding the latency-associated peptide of TGF- β 1 cause Camurati-Engelmann disease. *Nat. Genet.* **26**, 273–275 (2000).
32. Janssens, K., ten Dijke, P., Ralston, S.H., Bergmann, C. & Van Hul, W. Transforming growth factor- β 1 mutations in Camurati-Engelmann disease lead to increased signaling by altering either activation or secretion of the mutant protein. *J. Biol. Chem.* **278**, 7718–7724 (2003).
33. Mendias, C.L. *et al.* Transforming growth factor- β induces skeletal muscle atrophy and fibrosis through the induction of atrogen-1 and scleraxis. *Muscle Nerve* **45**, 55–59 (2012).
34. Zhou, X. *et al.* Reversal of cancer cachexia and muscle wasting by ActRIIB antagonism leads to prolonged survival. *Cell* **142**, 531–543 (2010).
35. McPherron, A.C., Lawler, A.M. & Lee, S.J. Regulation of skeletal muscle mass in mice by a new TGF- β superfamily member. *Nature* **387**, 83–90 (1997).
36. Bogdanovich, S. *et al.* Functional improvement of dystrophic muscle by myostatin blockade. *Nature* **420**, 418–421 (2002).

ONLINE METHODS

Animals. Female athymic nude mice were obtained from Harlan (Indianapolis, IN) and female CB.17 SCID mice were obtained from Charles River (Hollister, CA) at 5 weeks of age. 6-week-old male CED and littermate control animals were used for experiments. All experiments with animals were performed at Indiana University and approved by Indiana University's Institutional Animal Care and Use Committee (IACUC). Each animal experiment was performed once unless otherwise stated.

Ethics statement. In all studies, mice were handled and euthanized in accordance with approved institutional, national and international guidelines.

Materials. Recombinant human TGF- β 1 was purchased from R&D Systems. SD-208 was obtained from Epichem Pty Ltd (Bentley, WA). Zoledronic acid (Zometa) was obtained from Novartis (Cambridge, MA). Rycal S107 (S107-HCl, FW 245.77) was synthesized as previously described^{17,37}. Anti-TGF- β antibody clone 1D11.16.8 (1D11) and mouse IgG1 isotype control (MOPC-21; unknown specificity) were obtained from BioXCell (West Lebanon, NH). Nox4 inhibitor (GKT137831) was obtained from Ark Pharm, Inc. (Libertyville, IL). Antibodies: Anti-RyR (Affinity Bioreagents, cat. MA3-916, Golden, CO; 1:2,000), anti-Cys NO antibody (Sigma, cat. N0409, St. Louis, MO; 1:2,000), anti-calstabin antibody (Santa Cruz Biotechnology, cat. sc-6173, Santa Cruz, CA; 1:2,500), anti-DNP (Oxyblot, Millipore, Darmstadt, Germany; 1:250), anti-pSMAD3 (Abcam, cat. ab40854, Cambridge, UK; 1:1,000), anti-SMAD3 (Abcam, cat. 52903, Cambridge, UK; 1:1,000), anti-Nox4 (Abcam, cat. 109225, Cambridge, UK; 1:1,000), anti-GAPDH (Sigma, cat. G8795, St. Louis, MO; 1:500) and anti-tubulin (Sigma, cat. 8203, St. Louis, MO; 1:500 each). Fluo-4 a.m. and Fura-red were obtained from Invitrogen/Molecular probes (cat. F-14201 and cat. F-3020, Eugene, OR).

Cell culture. MDA-MB-231 breast cancer cells³⁸ (HTB-26, American Type Culture Collection (ATCC), Manassas, VA), MCF-7 breast cancer cells³⁹ (HTB-22, ATCC), ZR75-1 breast cancer cells⁴⁰ (CRL-1500, ATCC), PC-3 prostate cancer cells⁴¹ (CRL-1435, ATCC) and RWGT2 lung cancer cells^{15,42} (isolated from bone metastases by T.A.G. as reported¹⁵) were cultured in Dulbecco's modified Eagle's media (DMEM) (Hyclone, Logan, UT) containing 10% heat-inactivated FBS (FBS) (Hyclone). JJJN-3 multiple myeloma cells⁴³ (ACC 541, Deutsche Sammlung von Mikroorganismen und Zellkulturen GmbH) were cultured in RPMI 1640 (Invitrogen, Grand Island, NY) containing 10% heat-inactivated FBS. A549 cancer cells (CCL-185, ATCC) were cultured in 1640 RPMI (Hyclone) containing 10% heat-inactivated FBS. C2C12 myoblast cells (CRL-1772, ATCC) were cultured subconfluently in DMEM containing 10% heat-inactivated FBS. C2C12 myoblasts were differentiated into myotubes by culture in DMEM containing 2% heat-inactivated horse serum (HS) (Hyclone). All cells were maintained at 37 °C with 5% CO₂ in a humidified chamber. All cells were verified to be free of mycoplasma contamination via routine PCR testing. No independent verification was completed. Cells treated with recombinant human TGF- β 1 (R&D Systems, Minneapolis, MN) were starved in DMEM (no serum) for 16–20 h and 5 ng/ml TGF- β 1 was added to cells in DMEM.

In vivo models. Intracardiac inoculation of tumor cells was performed as previously described^{11,38} into 4-week-old female athymic nude mice. Tumor cells (MDA-MB-231 and A549) were trypsinized, washed twice and resuspended in PBS to a final concentration of 10⁵ cells in 100 μ l. 100,000 cells were inoculated into each animal. Animals were anesthetized with ketamine and xylazine and positioned ventral side up. MDA-MB-231 or A549 cells were inoculated into the left ventricle by percutaneous injection using a 26-gauge needle. Visualization of bright red blood entering the hub of the needle in a pulsatile fashion indicated a correct position in the left cardiac ventricle. Animals were euthanized at 4 weeks after inoculation.

Mammary fat pad tumor inoculation was performed on 4-week-old female athymic nude mice. Tumor cells (MDA-MB-231) were trypsinized, washed twice and resuspended in PBS to a final concentration of 10⁶ cells in 100 μ l. 1,000,000 cells were inoculated into each animal. Mice were anesthetized with ketamine and xylazine and inoculated in the upper mammary fat pad using a 27-gauge needle. Animals were euthanized at 4 weeks after inoculation.

Intra-tibial inoculation of tumor cells was performed on 4-week-old female CB.17 SCID mice. Tumor cells (JJN-3) were trypsinized, washed twice and resuspended in PBS to a final concentration of 10⁵ cells in 20 μ l. 100,000 cells were inoculated into each animal. Mice were anesthetized with ketamine and xylazine and inoculated in the proximal tibia using a 27-gauge needle. Animals were euthanized at 34 d after inoculation.

Radiography. Osteolytic lesions were analyzed by radiography using a Kubtec digital X-ray imager (Kubtec, Milford, CT). Mice were imaged in a prone position at 2.7 \times magnification. Osteolytic lesion area was quantified using BioQuant software v14.1.6 (Bioquant Image Analysis Corporation, Nashville, TN). The investigators were blinded to treatment of subjects.

Bone histology and histomorphometry. Forelimbs, hindlimbs and spines of the mice were collected upon euthanasia and fixed in 10% neutral buffered formalin for 48 h and decalcified in 10% EDTA for 2 weeks. After decalcification, tissues were processed in a Shandon Excelsior automated tissue processor (Thermo Fisher Scientific, Grand Island, NY) and embedded in paraffin wax for sectioning. Longitudinal, mid-sagittal sections 3.5 μ m in thickness from the tibia, femur, humerus and lumbar spines were cut using an automated Microm HM 355 S microtome (Thermo Fisher Scientific). Tissue sections were stained with hematoxylin and eosin (H&E) and prepared for histomorphometric analysis. All sections were viewed on a Leica DM2500 compound microscope (W. Nuhsbaum Inc., McHenry, IL) with Q-imaging micropublisher cooled CCD color digital camera. Images were captured and analyzed using BioQuant software v14.1.6 (Bioquant Image Analysis Corporation). Tumor burden per mouse, defined as the area of bone occupied by the cancer cells, was calculated at the tibia, femur and humerus at 50 \times magnification on H&E-stained sections, as previously described³⁸. Osteoclast number at the tumor-bone interface (OCL/mm bone surface) in the femur, tibia and humerus was measured on tartrate-resistant acid phosphatase (TRAP)-stained slides at 200 \times magnification. The investigators were blinded to treatment of subjects.

Dual energy X-ray absorptiometry. Body composition was determined using a PIXImus mouse densitometer (GE Lunar II, Faxitron Corp., Tucson, AZ). The densitometer was calibrated with a plastic-embedded mouse phantom before use. Mice were anesthetized and placed on an adhesive tray in a prone position with limbs spread. Total body measurement was performed excluding the calvarium, mandible and teeth. Values were expressed as percentage change over baseline scan. The investigators were blinded to treatment of subjects.

Micro-computed tomography measurement of cross-sectional muscle area (muscle method). Mouse legs from control and tumor-inoculated mice were scanned using a VIVACT40 (SCANCO Medical, Wayne, PA) to measure muscle cross-sectional area. Both the tumor inoculated and the contralateral legs were scanned starting at the level of the tibio-fibular joint for 4–5-mm length under general inhalation anesthesia. Scanning parameters of 45 kVp, 133 μ A and 620-ms integration time were used as a standard setting to optimize the contrast between muscle and fat tissue. Lower muscle cross-sectional area was reported as the difference between the inoculated versus the contralateral control. The investigators were blinded to treatment of subjects.

Micro-computed tomography (micro-CT) (bone method). microCT imaging was performed on the distal femur and the proximal tibia using a VIVACT-40 (Scanco Medical). Scans were acquired using a 17.5- μ m³ isotropic voxel size, 55-kVp peak X-ray tube potential, 200-ms integration time and were subjected to Gaussian filtration. Total bone volume was evaluated at the distal epiphysis and metaphysis of the femur in a region that spanned 3.5 mm and at the proximal epiphysis and metaphysis of the tibia in a region that spanned 2.8 mm. A threshold of 160 was used to manually delineate bone from surrounding soft tissue. The investigators were blinded to treatment of subjects.

Grip strength. Forelimb grip strength was assessed by allowing each mouse to grab a wire mesh attached to a force transducer (Bioseb, Vitrolles, France) that records the peak force generated as the mouse is pulled by the tail horizontally

away from the mesh^{13,44}. We performed three consecutive pulls separated by 5-s pauses between each pull. We calculated the absolute grip strength (in grams) as the average of the peak forces recorded from the three pulls. The investigators were blinded to treatment of subjects.

Muscle function. *Ex vivo* contractility of the extensor digitorum longus (EDL) muscles was determined as previously described^{10,44}. EDL were dissected from the hind limbs and stainless-steel hooks were tied to the tendons of the muscles using 4-0 silk sutures and the muscles were mounted between a force transducer (Aurora Scientific, Aurora, ON, Canada) and an adjustable hook. The muscles were immersed in a stimulation chamber containing O₂/CO₂ (95/5%) bubbled Tyrode solution (121 mM NaCl, 5.0 mM KCl, 1.8 mM CaCl₂, 0.5 mM MgCl₂, 0.4 mM NaH₂PO₄, 24 mM NaHCO₃, 0.1 mM EDTA, 5.5 mM glucose). The muscle was stimulated to contract using a supramaximal stimulus between two platinum electrodes. Data was collected via Dynamic Muscle Control/Data Acquisition (DMC) and Dynamic Muscle Control Data Analysis (DMA) programs (Aurora Scientific). At the start of each experiment the muscle length was adjusted to yield the maximum force. The force-frequency relationships were determined by triggering contraction using incremental stimulation frequencies (0.5-ms pulses at 1–150 Hz for 350 ms at supramaximal voltage). Between stimulations the muscle was allowed to rest for 3 min. At the end of the force measurement, the length (L_0) and weight of the muscle were measured and the muscle was snap frozen in liquid N₂. To quantify the specific force, the absolute force was normalized to the muscle size, specifically the cross-sectional area, calculated as the muscle weight divided by the length using a muscle density constant of 1.056 kg/m³ (ref. 45). The investigators were blinded to treatment of subjects.

Calcium imaging in muscle fibers. Single flexor digitorum brevis (FDB) fibers were isolated by enzymatic dissociation as previously described⁴⁶. FDB muscles from the hind limb were incubated for 2 h at 37 °C in Dulbecco's Modified Eagles Medium (DMEM) containing 0.3% collagenase 1 (Sigma) and 10% FBS. The muscles were transferred to fresh DMEM and gently triturated using a 1,000 μ l pipette until the muscles were dissociated. The cell suspension was stored in an incubator at 37 °C and 5% CO₂ until the start of the experiment. FDB fibers were loaded with the fluorescent Ca²⁺ indicator Fluo-4 AM (5 μ M, Invitrogen/Molecular probes) for 15 min in room temperature (RT). The cells were allowed to attach to a laminin-coated glass cover slip that formed the bottom of a perfusion chamber. The cells were then superfused with tyrode solution (121 mM NaCl, 5.0 mM KCl, 1.8 mM CaCl₂, 0.5 mM MgCl₂, 0.4 mM NaH₂PO₄, 24 mM NaHCO₃, 0.1 mM EDTA, 5.5 mM glucose) bubbled with O₂/CO₂ (95/5%). The fibers were triggered to tetanic contraction using electrical field stimulation (pulses of 0.5 ms at supra-threshold voltage, at 70 Hz for 350 ms) and Fluo-4 fluorescence was monitored using confocal microscopy (Zeiss LSM 5 Live, 40 \times oil immersion lens, excitation wavelength was 488 nm and the emitted fluorescence was recorded between 495 nm and 525 nm) in line-scan mode. Only cells that were firmly attached to the glass bottom dish throughout the tetanic stimulation were included in the analysis. After subtraction of background fluorescence, the change in fluorescent signal during the tetanus (peak-resting (ΔF)) was divided by the resting signal ($\Delta F/F_0$). All experiments were performed at RT (approximately 20 °C).

Alternatively, basal Ca²⁺ was measured simultaneously with tetanic Ca²⁺, using ratiometric imaging with Fluo-4 (excited at 488 nm and emission collected at 505–530 nm) and Fura-red (Invitrogen/Molecular probes, excited at 488 nm and emission collected at >650 nm) imaging in cells ($F_{650\text{ nm}}/F_{515\text{ nm}}$). For this method basal Ca²⁺ concentration is shown with tetanic Ca²⁺ concentration. The investigators were blinded to treatment of subjects.

Proteomics. Skeletal muscle samples (tibialis anterior) were solubilized by ground glass homogenization and brief sonication in lysis buffer (8 M urea, 10 mM DTT solution freshly prepared). The homogenates were centrifuged at 150,000g for 20 min at 4 °C to remove insoluble materials. Protein concentration was determined by the Bradford Protein Assay. Protein reduction, alkylation and tryptic digestion were carried out using a conventional method previously published⁴⁷. The proteolyzed protein samples were injected onto a C18 reversed-phase column and analyzed using a Thermo-Finnigan linear

ion-trap (LTQ) mass spectrometer coupled with a Surveyor autosampler and a MS-HPLC system (Thermo-Finnigan). The acquired data were searched against the UniProt mouse protein sequence database containing 55,191 protein sequences (released on April 18, 2012) using SEQUEST (v. 28 rev. 12) algorithms in Bioworks (v. 3.3). Differential and post-translational modification on cysteine of +29 a.m.u. was included to identify the site of nitrosylation (C-NO) or oxidation (C-O3H). Identified peptides and proteins and their modification were validated by PeptideProphet, and ProteinProphet, in the Trans-Proteomic Pipeline (TPP, v. 3.3.0) (<http://tools.proteomecenter.org/software.php>)^{48,49}. Only proteins with probability ≥ 0.9000 and peptides with probability ≥ 0.8000 were reported. Protein quantification was performed using IdentiQuantXL software as described⁵⁰.

Measurement of protein oxidation and ROS production. To determine channel oxidation the carbonyl groups on the protein side chains were derivatized to 2,4-dinitrophenylhydrazone (DNP-hydrazone) by reaction with 2,4-dinitrophenylhydrazine (DNPH) (Oxyblot, Millipore, Darmstadt, Germany). The DNP signal on RyR1 was detected by immunoblotting with an antibody specific to DNP (Millipore, Darmstadt, Germany). Protein carbonyl concentration in tissue lysates was determined using the OxiSelect Protein Carbonyl ELISA Kit (Cell BioLabs, Inc., San Diego, CA). Briefly, 0.5 mg of EDL lysate was added to a 96-well protein-binding plate, which was incubated overnight at 4 °C. After washing the plate three times with PBS, the protein carbonyl groups were derivatized with DNPH for 45 min at room temperature (in the dark). Plates were developed with a DNP-specific antibody followed by a HRP-conjugated secondary antibody. Protein carbonyl concentration was determined by comparison with a standard curve of oxidized BSA. ROS production was determined in C2C12 myotubes using the OxiSelect *in vitro* ROS/RNS Assay kit (Cell BioLabs, Inc.). ROS production was measured using 0.25 mg of cell lysate according to the manufacturer's recommendations. For H₂O₂-treated cells, cells were incubated with 1 mM H₂O₂ for 30 min before lysis. The investigators were blinded to treatment of subjects.

RyR1 immunoprecipitation and immunoblotting. RyR1 oxidation and nitrosylation and calstabin1 binding was determined as previously described¹⁰. Extensor digitorum longus (EDL) muscles were isotonicly lysed in 0.5 ml of a buffer containing 50 mM Tris-HCl (pH 7.4), 150 mM NaCl, 20 mM NaF, 1.0 mM Na₃VO₄, and protease inhibitors. C2C12 cells were lysed in NP-40 lysis buffer containing 50 mM Tris-HCl (pH 8.0) 150 mM NaCl, 1.0% NP-40 and protease inhibitors. An anti-RyR antibody (4 μ g anti-RyR1 antibody 5029 (ref. 10), a custom antibody against the last nine amino acids (CRKQYEDQLS; a cysteine was added at the N terminus) of the rabbit skeletal muscle RyR1) was used to immunoprecipitate RyR1 from 250 μ g of tissue homogenate. Samples were incubated with antibody in 0.75 ml of a modified RIPA buffer (50 mM Tris-HCl pH 7.4, 0.9% NaCl, 5.0 mM NaF, 1.0 mM Na₃VO₄, 1% Triton-X100 and protease inhibitors) for 1 h at 4 °C. The immune complexes were incubated with protein A-sepharose beads (Sigma) overnight at 4 °C and the beads were washed twice with modified RIPA buffer. Proteins were separated on 4–12% Bis-Tris gels (Life Technologies) and transferred to nitrocellulose for 1 h at 100 V (Bio-Rad, Hercules, CA). After incubation with blocking solution to prevent nonspecific antibody binding, immunoblots were developed with anti-RyR (Affinity Bioreagents, cat. MA3-916, Golden, CO; 1:2,000) and anti-Cys-NO antibody (Sigma, cat. N0409, St. Louis, MO; 1:2,000) or an anti-calstabin antibody (Santa Cruz Biotechnology, cat. sc-6173, Santa Cruz, CA; 1:2,500). Immunoblots were developed and quantified using the Odyssey Infrared Imaging System (LICOR Biosystems, Lincoln, NE) and infrared-labeled secondary antibodies. Detection of pSMAD3, SMAD3, Nox4 (Abcam, Cambridge, UK; 1:1,000 each), GAPDH and tubulin (Sigma; 1:500 each) from mouse muscle, human biopsies and C2C12 cells was via lysis in NP-40 buffer and detection and quantification of immobilized proteins either using the Odyssey Infrared Imaging System or GE ImageQuant LAS4000 Imaging System (GE Healthcare Bio-sciences, Pittsburgh, PA). The investigators were blinded to treatment of subjects.

Human samples. Muscle biopsies from humans with breast and lung cancer and non-oncologic controls were obtained with consent under a research exempt waiver (IRB# 1403849213) approved by the institutional review board (IRB)

of Indiana University School of Medicine from the clinical research laboratory of P. Picci at the Istituto Ortopedico Rizzoli, Bologna, Italy. Control muscle samples were from humans with non-cancer-related musculoskeletal conditions. Humans with breast and lung cancer all had bone metastases and had not received chemotherapy at the time of tissue collection. Of the breast cancer patients, one also had lung metastases and one had tumor cells in the thyroid. Of the lung cancer patients, one also had cancer in the lymph nodes. This study was conducted under protocol approval from the IRB of Indiana University School of Medicine.

Drug treatments. All drug treatments were initiated 48 h before tumor cell inoculation with the exception of Rycal S107, which was initiated at the time of tumor cell inoculation.

SD-208. As described, SD-208 is a specific inhibitor of the TGF- β type I receptor⁵¹. SD-208 (60 mg/kg/d) or vehicle (1% methylcellulose) was administered by daily gavage and continued daily for the duration of each study.

Zoledronic acid. Zoledronic acid (ZA), an anti-resorptive bisphosphonate with FDA approval for use in humans with bone metastases, or vehicle (PBS) was administered by subcutaneous injection (5 μ g/kg) three times per week for the duration of each study.

TGF- β -specific antibody. Antibody clone 1D11.16.8 (1D11) is a neutralizing antibody to all three subtypes of TGF- β (TGF- β 1, TGF- β 2 and TGF- β 3). 1D11 (10 mg/kg) or isotype control (MOPC-21; 10 mg/kg) was administered by intraperitoneal injection three times per week for the duration of each study²⁴.

Rycal (S107). S107 is a benzothiazepine derivative that binds the RyR1 channel and enhances the binding affinity of calstabin1 (ref. 13). S107 was administered via osmotic infusion pump (Azlet) for continuous delivery. The mini-pump was implanted subcutaneously and the opening sutured and glued. Wounds were monitored for healing.

Nox4 inhibitor (GKT137831). GKT137831 (60 mg/kg/day) or vehicle (1.2% methylcellulose + 0.1% Polysorbate 80) was administered by daily gavage for the duration of the study.

Single-channel measurements. Muscles were homogenized using a Tissuemizer (Fisher Scientific) at the highest speed for 1 min with 2 volumes of: 20 mM Tris-maleate (pH 7.4), 1 mM EDTA and protease inhibitors (Roche). Homogenate was centrifuged at 4,000g for 15 min at 4 °C and the supernatant was centrifuged at 40,000g for 30 min at 4 °C. The final pellet, containing the SR fractions, was resuspended and aliquoted in 250 mM sucrose, 10 mM MOPS (pH 7.4), 1 mM EDTA and protease inhibitors. Samples were frozen in liquid nitrogen and stored at -80 °C. SR vesicles containing RyR1 were fused to planar lipid bilayers formed by painting a lipid mixture of phosphatidylethanolamine and phosphatidylcholine (Avanti Polar Lipids, Alabaster, AL) in a 3:1 ratio in decane across a 200- μ m hole in polysulfonate cups (Warner Instruments, Hamden, CT) separating two chambers. The *trans* chamber (1.0 ml), representing the intrasR (luminal) compartment, was connected to the head stage input of a bilayer voltage clamp amplifier. The *cis* chamber (1.0 ml), representing the cytoplasmic compartment, was held at virtual ground. Symmetrical solutions used were as follows: 1 mM EGTA, 250 mM HEPES, 125 mM Tris-HCl, 50 mM KCl, 0.64 mM CaCl₂ (pH 7.35) as *cis* solution and 53 mM Ca(OH)₂, 50 mM KCl, 250 mM HEPES (pH 7.35) as *trans* solution. The concentration of free Ca²⁺ in the *cis* chamber was calculated with WinMaxC program (version 2.50; <http://www.stanford.edu/~cpatton/maxc.html>). SR vesicles were added to the *cis* side and fusion with the lipid bilayer was induced by making the *cis* side hyperosmotic by the addition of 400–500 mM KCl. After the appearance of potassium and chloride channels, the *cis* side was perfused with the *cis* solution. Single-channel currents were recorded at 0 mV by using a Bilayer Clamp BC-525C (Warner Instruments), filtered at 1 kHz using a Low-Pass Bessel Filter 8 Pole (Warner Instruments) and digitized at 4 kHz. All experiments were performed at room temperature (23 °C). Data acquisition was performed by using Digidata 1322A and Axoscope 10.1 software (Axon Instruments, Sunnyvale, CA). The recordings were analyzed by using Clampfit 10.1 (Molecular Devices, Sunnyvale, CA) and Origin software (ver. 6.0, Microcal Software). The investigators were blinded to the genotype, age and treatment of the groups. Single-channel currents were measured at 150 nM cytosolic [Ca²⁺] using Ca²⁺ as a charge carrier at 0 mV. Channel openings are shown as upward deflections; the closed (c-) state of the

channel is indicated by horizontal bars in the beginning of each trace. P_o , open probability; T_o , average open time; T_c , average closed time. The activity of the channel, indicated by the thick black bar, is shown on the expanded time scale. The investigators were blinded to treatment of subjects.

SERCA activity. SERCA activity was measured using the malachite green procedure for phosphate determination, adapted to the microscale as previously described⁵². The reaction was started by the addition of 50 μ g of EDL microsomes to 150 μ l of reaction mixture (20 mM MOPS, Tris-HCl, pH 6.8, 100 mM KCl, 5 mM MgCl₂, 5 mM ATP, 1 mM EGTA, 0.350 mM CaCl₂ (free Ca²⁺ concentration of approximately 500 nM as calculated using the CHELATOR program). After 5 min, the reaction was stopped by the transfer of 120 μ l of reaction mixture to 80 μ l of malachite green reagent mixture in a 96-well microplate. The malachite green reagent mixture was made by mixing 0.122% malachite green hydrochloride in 6.2 N H₂SO₄, 5.76% ammonium paramolybdate tetrahydrate and 11% Tween-20 in a volume ratio of 100:66:2. Color development was quenched after 10 s by the addition of 45 μ l of 15.1% sodium citrate dihydrate. Inorganic phosphate liberated in the ATPase reaction was quantified by comparison of absorbance at 570 nm with standard curves generated with known amounts of Na₂HPO₄ in the reaction buffer. The investigators were blinded to treatment of subjects.

Enzyme-linked immunosorbent assay (ELISA). ELISA assay for TGF- β quantification from mouse serum was performed using Quantikine human TGF- β 1 (R&D Systems; Minneapolis, MN; USA) according to manufacturer's guidelines. Serum samples were diluted 1:20. ELISA plates were analyzed by absorbance reading using a microplate reader set to 450 nm with wavelength correction set to 540 nm. Investigators were blinded to sample identity.

Caloric restriction. Caloric restriction was determined by measuring food intake by mice with MDA-MB-231 breast cancer bone metastases as an average amount of food in grams (calculated by per cage basis; $n = 5$ mice per cage). Food was restricted to healthy animals ($n = 10$ per group; strain, age and sex matched to bone metastasis model) for 1 week following 3 weeks of *ad libitum* feeding to maintain consistency with previous animal studies. Calculated feedings (30–40% reduction of normal intact) and body weight measurements were completed at the same time each day. The investigators were blinded to treatment of subjects.

Calcium sparks measurements. C2C12 cells were incubated in a relaxing solution (140 mM potassium glutamate, 10 mM HEPES, 10 mM MgCl₂, 0.1 mM EGTA, pH 7.0). Cells were permeabilized in relaxing solution containing 0.01% saponin for ~30 s. After washing the sample with a saponin-free solution, the solution was changed to an internal medium (140 mM potassium glutamate, 5 mM Na₂ATP, 10 mM glucose, 10 mM HEPES, 4.4 mM MgCl₂, 1.1 mM EGTA, 0.3 mM CaCl₂, Fluo-3 (pentapotassium salt, Invitrogen/Molecular probes, pH 7.0)) for Ca²⁺ sparks acquisition as previously reported¹³. Fluorescence images were acquired with a Zeiss LSM 5 Live confocal system (63 \times oil immersion, NA = 1.4) operated in line-scan mode (x versus t , 1.5 ms/line, 3,000 lines per scan) along the longitudinal axis of the fibers. Each location was scanned at most twice before moving the line location. Fluo-3 was excited with an Argon laser at 488 nm, and the emitted fluorescence was recorded between 495 and 555 nm. Image analysis was performed using custom made routines compiled in IDL (v7.1, ITT). Potential Ca²⁺ spark areas were empirically identified using an autodetection algorithm⁵³. The mean F value for the image was calculated by summing and averaging the temporal F at each spatial location while ignoring potential spark areas. This F value was then used to create a F/F image pixel by pixel. Statistical comparisons were performed using the ANOVA test with a significance level set at $P < 0.05$. The investigators were blinded to the treatment of subjects.

Semi-quantitative RT-PCR. Tibialis anterior (TA) muscle was lysed by Dounce homogenization in Trizol (Invitrogen) for RNA extraction. One-fifth volume of chloroform was added to the lysates, which were then vortexed vigorously for 15 s and incubated at room temperature for 3 min. Samples were centrifuged (12,000g, 15 min, 4 °C) and the upper aqueous phase was collected and loaded

onto a GenElute mammalian total RNA mini column (Sigma). Total RNA was isolated according to the manufacturer's instructions. DNase I treatment was performed to remove genomic DNA contamination (Qiagen), and RNA integrity was assessed on agarose gels. RNA (500 ng per sample) was reverse-transcribed using Superscript II (Invitrogen) according to the manufacturer's instructions with anchored oligo(dT) (Promega) for priming. The resulting cDNAs were prepared for semiquantitative real-time PCR using HotStart-IT SYBR Green PCR Kit (Affymetrix) and analyzed in a CFX96 Real-Time PCR Detection System (BioRad) for 40 cycles (95 °C for 15 s, 58 °C 30 s, 72 °C for 30 s) after an initial 2 min incubation at 95 °C. Primers were optimized for real-time PCR (amplification efficiency 100 ± 5%). Target gene expression (*Nox1*, *Nox2* and *Nox4*) was normalized against the housekeeping gene β 2-microglobulin (*B2m*), and data were analyzed using the $\Delta\Delta C_t$ method.

Primers: *B2m* forward: 5'-CTGACCGGCTGTATGCTAT-3'; *B2m* reverse 5'-CAGTCTCAGTGGGGGTGAAT-3'; *Nox1* forward 5'-AATGCCCA GGATCGAGGT-3'; *Nox1* reverse 5'-GATGGAAGCAAAGGGAGTGA-3'; *Nox2* forward 5'-CCCTTTGGTACAGCCAGTGAAGAT-3'; *Nox2* reverse 5'-CAATC CCGGCTCCCACTAACATCA-3'; *Nox4* forward 5'-GGATCACAGAAGGT CCCTAGCAG-3'; *Nox4* reverse 5'-GCGGCTACATGCACACCTGAGAA-3'.

Statistical analyses. The data are presented as mean ± s.e.m. The group size for *in vivo* experiments was determined by power analyses using previous muscle-specific force data to achieve statistical significance with the fewest mice. The mean difference in muscle-specific force in mice with breast cancer versus non-tumor was 42% (275 kN/m² versus 390 kN/m²; s.d. = 64; **Fig. 1b**). Assuming α error rate = 0.05 and β = 0.20 and a conservative 30% mean difference (275 to 360), the minimum number of animals per group is $n = 10$. Differences among experimental groups were analyzed by *t*-tests or analysis of variance (ANOVA) with appropriate post hoc and multiple comparison tests. For single-timepoint measures of any sample size, a two-sided Student's *t*-test was used⁵⁴. When more than two groups were compared simultaneously, analysis of variance (ANOVA) followed by Tukey's post hoc tests were used (e.g., comparison between control, tumor bearing and tumor bearing + S107 groups). In some experiments measurements in a group were repeated over time (e.g., forelimb grip). These experiments were analyzed by repeated measures ANOVA followed by Tukey's post hoc tests. *P* values less than 0.05 were considered significant (**P* < 0.05; ***P* < 0.01; ****P* < 0.0005; *****P* < 0.0001). Statistical analyses were performed with Prism 6.0 software (GraphPad Prism, La Jolla, CA). Samples for semi-quantitative RT-PCR were analyzed with a minimum of three biological replicates. Samples for western blotting and RT-PCR were analyzed in biological triplicate (minimum). All sample sizes reported in study are minimum values. Assumptions for ANOVA analyses were met (i.e., normal distribution) with the exception of data in **Figures 1c, 2e, 4f and 5a,b**. For these analyses, we used a nonparametric (Kruskal-Wallis) ANOVA and Dunn's multiple comparisons. Variation between groups being compared was not measured due to variability in tumor progression in mice. Exclusion plan: EDL specific force data was excluded in cases in which there was evidence of damage to the muscle fibers. Forelimb

grip strength data was excluded when there was evidence of forearm bone lesions as pain is likely to have a role in forelimb grip strength and animal compliance. This exclusion plan was pre-established. Female athymic nude mice obtained from Harlan and female CB.17 SCID mice obtained from Charles River were randomized into groups upon arrival. All statistical tests use biological replicates and are indicated by group size (*n*) in figure legends. Investigators were blinded to the identity of subjects.

37. Wehrens, X.H. *et al.* Protection from cardiac arrhythmia through ryanodine receptor-stabilizing protein calstabin2. *Science* **304**, 292–296 (2004).
38. Dunn, L.K. *et al.* Hypoxia and TGF- β drive breast cancer bone metastases through parallel signaling pathways in tumor cells and the bone microenvironment. *PLoS ONE* **4**, e6896 (2009).
39. Soule, H.D., Vazquez, J., Long, A., Albert, S. & Brennan, M. A human cell line from a pleural effusion derived from a breast carcinoma. *J. Natl. Cancer Inst.* **51**, 1409–1416 (1973).
40. Yin, J.J. *et al.* A causal role for endothelin-1 in the pathogenesis of osteoblastic bone metastases. *Proc. Natl. Acad. Sci. USA* **100**, 10954–10959 (2003).
41. Hu, Z. *et al.* Systemic delivery of oncolytic adenoviruses targeting transforming growth factor- β inhibits established bone metastasis in a prostate cancer mouse model. *Hum. Gene Ther.* **23**, 871–882 (2012).
42. Johnson, R.W. *et al.* Wnt signaling induces gene expression of factors associated with bone destruction in lung and breast cancer. *Clin. Exp. Metastasis* **31**, 945–959 (2014).
43. Jackson, N. *et al.* Two new IgA1- κ plasma cell leukaemia cell lines (JJN-1 & JJN-2) which proliferate in response to B cell stimulatory factor 2. *Clin. Exp. Immunol.* **75**, 93–99 (1989).
44. Bonetto, A., Andersson, D.C. & Waning, D.L. Assessment of muscle mass and strength in mice. *Bonekey Rep.* **4**, 732 (2015).
45. Yamada, T. *et al.* Impaired myofibrillar function in the soleus muscle of mice with collagen-induced arthritis. *Arthritis Rheum.* **60**, 3280–3289 (2009).
46. Aydin, J. *et al.* Increased mitochondrial Ca²⁺ and decreased sarcoplasmic reticulum Ca²⁺ in mitochondrial myopathy. *Hum. Mol. Genet.* **18**, 278–288 (2009).
47. Lai, X. *et al.* Characterization of the renal cyst fluid proteome in autosomal dominant polycystic kidney disease (ADPKD) patients. *Proteomics Clin. Appl.* **2**, 1140–1152 (2008).
48. Keller, A., Nesvizhskii, A.I., Kolker, E. & Aebersold, R. Empirical statistical model to estimate the accuracy of peptide identifications made by MS/MS and database search. *Anal. Chem.* **74**, 5383–5392 (2002).
49. Nesvizhskii, A.I., Keller, A., Kolker, E. & Aebersold, R. A statistical model for identifying proteins by tandem mass spectrometry. *Anal. Chem.* **75**, 4646–4658 (2003).
50. Lai, X., Wang, L., Tang, H. & Witzmann, F.A. A novel alignment method and multiple filters for exclusion of unqualified peptides to enhance label-free quantification using peptide intensity in LC-MS/MS. *J. Proteome Res.* **10**, 4799–4812 (2011).
51. Mohammad, K.S. *et al.* Pharmacologic inhibition of the TGF- β type I receptor kinase has anabolic and anti-catabolic effects on bone. *PLoS ONE* **4**, e5275 (2009).
52. Kimura, Y., Kurzydowski, K., Tada, M. & MacLennan, D.H. Phospholamban regulates the Ca²⁺-ATPase through intramembrane interactions. *J. Biol. Chem.* **271**, 21726–21731 (1996).
53. Cheng, H. *et al.* Amplitude distribution of calcium sparks in confocal images: theory and studies with an automatic detection method. *Biophys. J.* **76**, 606–617 (1999).
54. de Winter, J.C.F. Using the Student's *t*-test with extremely small sample sizes. *Pract. Assess., Res. Eval.* **18**, 1–12 (2013).